A crystal plasticity model for describing the anisotropic hardening behavior of steel sheets during strain-path changes

Hwigeon Kim[1], Frédéric Barlat[1], Yongmoon Lee[1], Shakil Bin Zaman[2], Chong Soo Lee[1], Youngung Jeong[3*]

[1]Graduate Institute of Ferrous Technology (GIFT), Pohang University of Science & Technology (POSTECH), 77 Cheongam-ro, Nam-gu, Pohang, Gyeongbuk, Republic of Korea

[2]University of Twente, Faculty of Engineering Technology, 7500 AE Enschede, The Netherlands.

[3]Changwon National University, 20 Changwondaehak-ro Changwon, Gyeongnam, Republic of Korea

*Corresponding author

Email: yjeong@changwon.ac.kr, Tel: +82-55-213-3694, Fax: +82-55-261-7017

Abstract

In the present study, a viscoplastic self-consistent crystal plasticity model (VPSC-RGBV), which accounts for various microstructural features, including the accumulation and annihilation of dislocations due to slip activity and latent hardening originated from interactions between gliding dislocations on different slip planes, is described. The simulation results of the VPSC-RGBV model are compared with those of a macro-mechanical distortional plasticity model, the so-called homogeneous anisotropic hardening (HAH), and experimental data pertaining to metals undergoing complex loading histories. The differences between the simulated and experimental results under non-proportional loading, including 1) the stress-strain curve, 2) instantaneous r-value after strain-path change, and 3) yield surface evolution, are discussed. Finally, potential improvements are suggested for VPSC-RGBV model.

Keywords: A microstructures; B crystal plasticity; B constitutive behavior; C optimization; strain-path change

1. Introduction

During sheet forming operations, even though blank sheet metal may be subjected to a complex loading history, its strain hardening behavior is often characterized on the basis of simple mechanical experiments, in which the material is subjected to monotonic loading. In addition, the strain hardening description is often assumed to follow an isotropic hardening law. However, the stress-strain curves obtained from mechanical experiments conducted under complex loading conditions generally exhibit various anisotropic features including, but not limited to 1) Bauschinger effect, 2) drastic changes in the hardening rate, and 3) permanent softening or hardening different from those obtained under a monotonic loading condition. Various experimental studies demonstrated that the three aforementioned anisotropic elements are significantly affected by the amount of prestrain and degree of path change (Barlat et al., 2003a; Ha et al., 2013; Nesterova et al., 2001; Vincze et al., 2005).

Therefore, for an accurate description of material behavior under forming operations, mechanical properties sensitive to path change should be accounted for. For instance, for predicting the springback, accurate modeling of the stress-strain response under complex loading scenarios is critical (Choi et al., 2016; Lee et al., 2011, 2012a; Yoshida and Uemori, 2003). Furthermore, formability is also very sensitive to strain-path change (Stoughton, 2000).

The kinematic hardening rule is often used by the metal-forming community to describe flow curves under complex loading scenarios. Combined isotropic and kinematic hardening rules are often adopted in various metal forming simulations using finite element (FE) software. Many studies have shown that macro-mechanical constitutive models based on the kinematic hardening rule can lead to a reasonable prediction accuracy for springback (Cardoso and Yoon, 2009, 2008; Chung et al., 2005; Geng and Wagoner, 2002; Lee et al., 2005a,b, 2007; Yoshida et al., 2002). It should be noted that the mentioned studies mainly focus on load reversal, where Bauschinger effect prevails. However, if a material undergoes strain-path changes, in which new slip systems are activated, latent hardening and cross-hardening effects appear, which are not well described by the kinematic hardening rule. Moreover, various experimental studies demonstrate that kinematic hardening, in which the yield surface translates in stress space, does not accurately describe anisotropic hardening (Khan 2009, 2010a,b).

To describe anisotropic hardening behavior under more general loading scenarios, alternative approaches using distortional plasticity have been proposed (Barlat et al., 2011; Ortiz and Popov, 1983; Voviadjis et al., 1995). Barlat et al.'s study focuses on the Homogeneous Anisotropic Hardening (HAH) model (Barlat et al., 2011), which completely eliminates the contribution of the kinematic component. The HAH model was successfully implemented in FE code (Lee et al., 2012a) and springback simulations after U-draw bending were found to be in good agreement with the experimental results (Lee et al., 2012b). Based on an understanding of the dislocation structure evolution, HAH with a Yld2000-2d anisotropic yield function (HAH-Yld2000-2d) was extended to account for the latent hardening observed in materials subjected to cross-loading (Barlat et al., 2003b,

2013, 2014). Furthermore, Zaman et al. (2017) successfully analyzed the behavior of sheet metals subjected to several additional loading scenarios using the HAH-Yld2000-2d model.

Despite the successful applications mentioned above, industrial usage of the HAH model is still a challenge as the characterization of its constitutive parameters generally requires various mechanical experiments, which cannot be easily performed. Although the behavior of certain evolving state variables in the HAH model was developed by considering microstructural effects, the constitutive parameters are not directly related to features such as the crystallographic texture, slip systems, and dislocation density. Therefore, in principle, the parameter set obtained from a material is not reusable, even for a similar material.

Various studies show that changes in the strain path affect the evolution of dislocation-related microstructures, leading to changes in the macro-mechanical response of materials (Beyerlein and Tomé, 2007; Kitayama et al., 2013; Knezevic et al., 2013; Peeters et al., 2002; Rauch et al., 2007, 2011, Wen et al., 2016). Of the mentioned models, the viscoplastic self-consistent crystal plasticity framework (VPSC) (Lebensohn et al., 2007), which was developed by Kitayama et al. (2013) to incorporate the dislocation-based hardening model called RGBV, which was in turn proposed by Rauch et al. (2011), is considered in the current study. Later, this crystal plasticity model (denoted as VPSC-RGBV) was improved by Wen et al. (2016) to account for the back-stress pertaining to individual slip systems. It was recently shown that the VPSC-RGBV model leads to a distortional behavior of the yield surface similar to experimental observations and to predictions by the HAH model (Jeong et al., 2016).

The application of the VPSC-RGBV model has so far been limited to single-phase materials, such as BCC-low carbon steel (Jeong et al., 2016; Kitayama et al., 2013; Wen et al., 2016) and HCP magnesium alloys (Wen et al., 2015). As various alloys that are widely used in industrial sections nowadays consist of two or more phases, it is important to investigate the applicability of the VPSC-RGBV model to an actual multiphase alloy. To this end, the current study investigates the behavior of a dual-phase DP780 steel sample with reference to a single-phase CHSP45R alloy in order to

understand the limits and advantages of the VPSC-RGBV model. The predictive accuracy and material characterization of the VPSC-RGBV model are discussed in detail with respect to the HAH model.

The outline of this article is as follows. Section 2 provides details on the mechanical experiments and microstructural characterization. In Section 3, the main features of the VPSC-RGBV and HAH models are introduced. Section 4 addresses the numerical determination of the constitutive parameters pertaining to the VPSC-RGBV model. In Section 5, the validity of the VPSC-RGBV model is investigated by comparing the experimental and predicted behavior of two steels, DP780 and CHSP45R. In addition, the predictive accuracy of the VPSC-RGBV model is compared with that of the HAH model. Section 6 provides a detailed discussion regarding the experimental and simulation results obtained in this investigation. Finally, Section 7 concludes this study and highlights aspects that require special attention and more research in the future.

2. Experimental

2.1 Materials

Two different grades of sheet materials, namely, single-phase CHSP45R and dual-phase DP780, were investigated. Single-phase CHSP45R is a cold-rolled steel, which can be classified as a high-strength steel (HSS). Dual-phase DP780 combines a soft ferrite matrix with hard martensitic particles, leading to high strength with good ductility.

2.2 Mechanical tests

All the mechanical tests were conducted in a separate work (Zaman et al., 2017). In what follows, only those experimental conditions relevant to the current investigation are discussed.

Table 1 lists the mechanical properties of CHSP45R and DP780 steels obtained under uniaxial tension according to the ASTM E8 standards. The tests were repeated along three different angles

with respect to the rolling direction. The three different directions are also referred to as RD, DD, and TD, corresponding to the angular values of 0°, 45°, and 90°, respectively.

Table 1 Mechanical properties of CHSP45R and DP780 from uniaxial tension tests (Zaman et al., 2017)

CHSP45R (1.2t)			
Direction	Young's modulus [GPa]	Yield stress [MPa]	R-value
0°	165	334	1.07
45°	165	331	1.36
90°	165	345	0.95

DP780 (1.0t)			
Direction	Young's modulus [GPa]	Yield stress [MPa]	R-value
0°	185	548	0.70
45°	185	506	0.97
90°	185	534	0.82

In addition to the uniaxial mechanical properties listed in Table 1, experimental data obtained from five mechanical tests were utilized in the current work. More specifically, these experiments were a) uniaxial tension along TD followed by uniaxial compression along TD, b) uniaxial tension initially along TD and then RD, c) uniaxial tension along TD and then DD, d) uniaxial tension along TD followed by biaxial tension with three different ratios of in-plane stress components, and e) biaxial tension with three different ratios of in-plane stress components performed on the as-received samples. Note that among these five, experiment e) is the only one where the as-received sample undergoes a monotonic loading. For the sake of brevity, experiments a) to e) are referred to as TDT-

TDC, TDT-RDT, TDT-DDT, TDT-BT, and BT, respectively. Note that TDT, RDT, and DDT stand for uniaxial tension in TD, RD, and DD respectively, whereas TDC and BT denote uniaxial compression in TD and the biaxial tension, respectively. Figs. 1 to 3 show schematic illustrations of these additional mechanical experiments. BT tests were conducted following the procedure described in Kuwabara et al. (1998) with three different force ratios using the cruciform sample shown in Fig. 2.

The same amount of TDT prestrain (i.e., 6% engineering strain) was applied to TDT-TDC, TDT-RDT, TDT-DDT, and TDT-BT. The amount of deformation imposed on the second loading segment was limited by either buckling or fracture. A large-scale steel specimen, as shown in Figs. 2 and 3, was used for the TDT prestrain in order to ensure that the gauge region of the subsequent test remained homogeneous. The stress and strain data were extracted from the uniaxial test results using a load cell and digital image correlation technique, respectively.

To quantify the severity of any arbitrary strain-path change, a parameter defined by Schmitt et al. (1985) was used:

$$\delta = \frac{d\boldsymbol{\varepsilon}^1 : d\boldsymbol{\varepsilon}^2}{\|d\boldsymbol{\varepsilon}^1\| \|d\boldsymbol{\varepsilon}^2\|} \qquad \text{Eq (1)}$$

where $d\boldsymbol{\varepsilon}^1$ and $d\boldsymbol{\varepsilon}^2$ are the strain increments in the first and second loading paths, respectively. The Schmitt parameter δ remains within the range of [–1, 1]. Certain δ values correspond to notable strain-path changes. For instance, $\delta = -1$ indicates strain reversal such as tension-compression (or vice versa), whereas $\delta = 0$ corresponds to cross-loading in which only new slip systems are presumably activated after strain-path change.

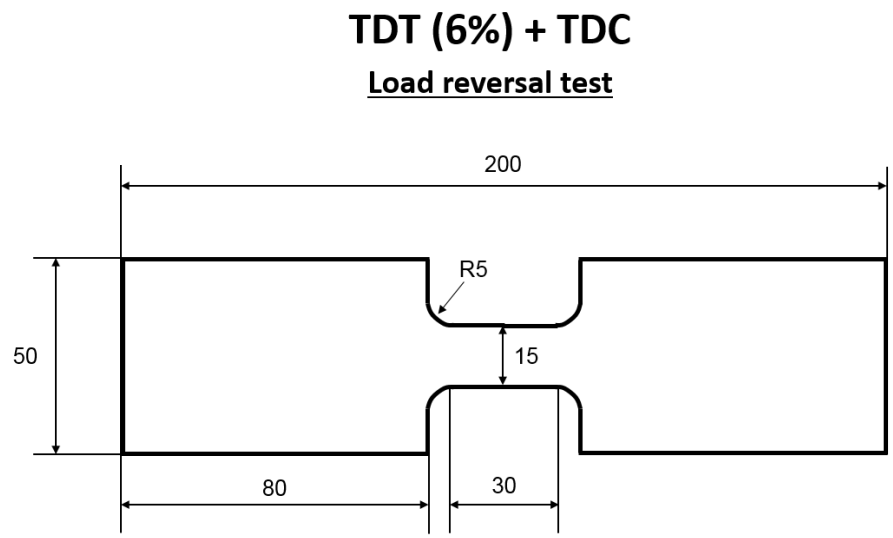

Fig. 1 Geometry of specimen for uniaxial tension along TD followed by uniaxial compression in TD

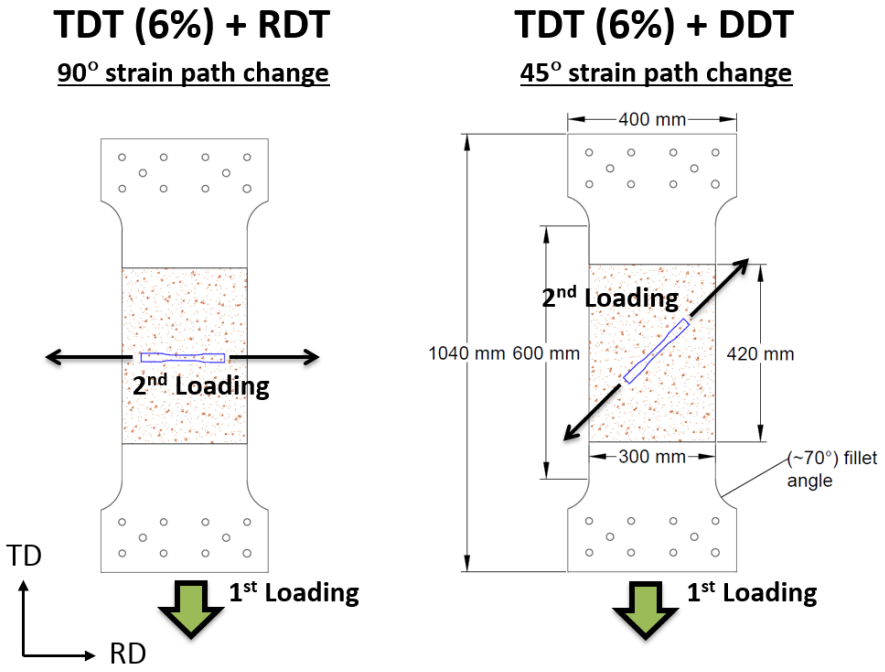

Fig. 2 Schematic view of two-step tension tests on large-scale specimens

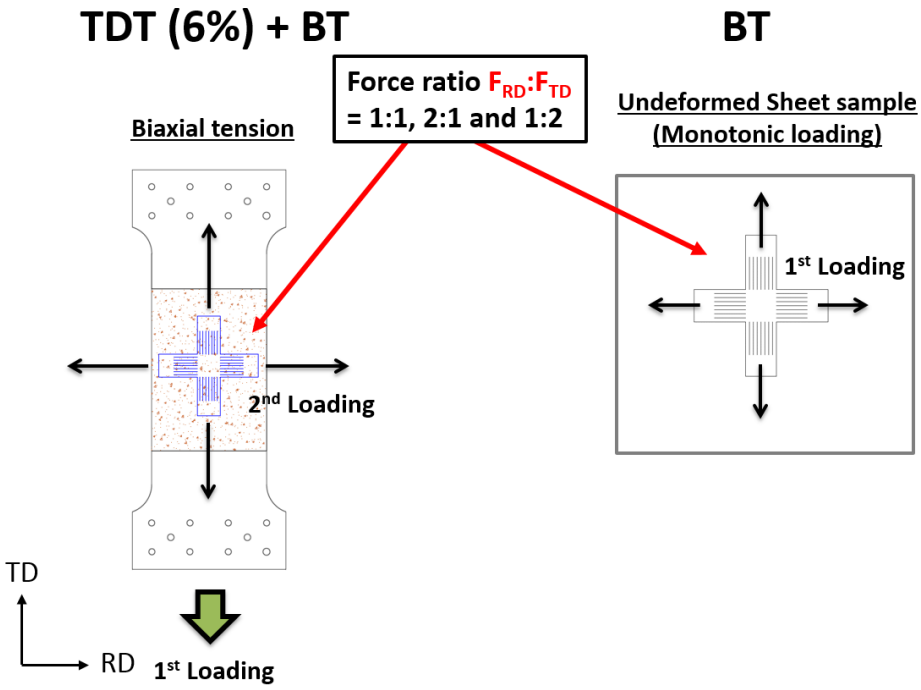

Fig. 3 Schematic view of the tension-biaxial tension and monotonic biaxial tests with three different force ratios

2.3 Microstructural characterization

X-ray diffraction (XRD) was performed on both DP780 and CHSP45R samples using a Bruker D8-Discover instrument with Cu K-α radiation to determine the crystallographic texture of the as-received samples. CHSP45R is a single-phase ferritic steel and its (110), (200), and (211) pole figures were measured. On the other hand, DP780 contains both ferritic and martensitic phases, whose diffraction patterns cannot be easily deconvoluted. Nevertheless, the same three pole figures were collected for DP780 but were considered as an average of both ferritic and martensitic phases. Background intensity was subtracted from the raw pole figures and a defocusing correction was performed. A texture analysis software, MTEX (Hielscher and Schaeben, 2008), was used to calculate the orientation distribution and the reconstructed (100), (110), and (111) pole figures are shown in Fig. 4.

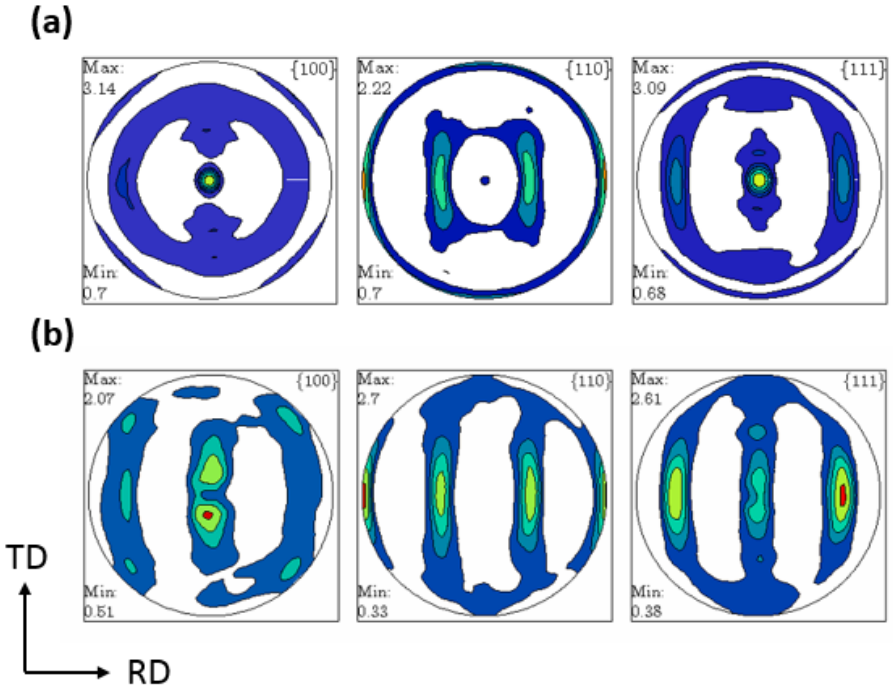

Fig. 4 (100), (110), and (111) pole figures of the (a) CHSP45R and (b) DP780 steels reconstructed from MTEX (Hielscher and Schaeben 2008) using experimental pole figures obtained from XRD

In addition to XRD, electron backscattered diffraction (EBSD) analysis was applied on DP780 to evaluate the crystallographic textures of ferrite and martensite. The specimen was electro-polished at 34 V with a solution of 5 % perchloric acid and acetic acid. Kernel average misorientation (KAM) was used to segment out martensitic regions from ferrite grains. Volume expansion accompanied by martensitic transformation may induce a high dislocation density around martensite (Pinard et al., 2013). Therefore, regions with relatively high dislocation densities (represented by high KAM values) are presumed to be martensite. Assuming that the critical KAM value is 1.5°, a ferrite-to-martensite ratio of 65:35 was obtained – see Fig. 5 for the corresponding KAM map. In the EBSD image, roughly 1000 and 400 grains were sampled for ferrite and martensite, respectively. Fig. 6 shows the (100), (110), and (111) pole figures reconstructed from the KAM analysis.

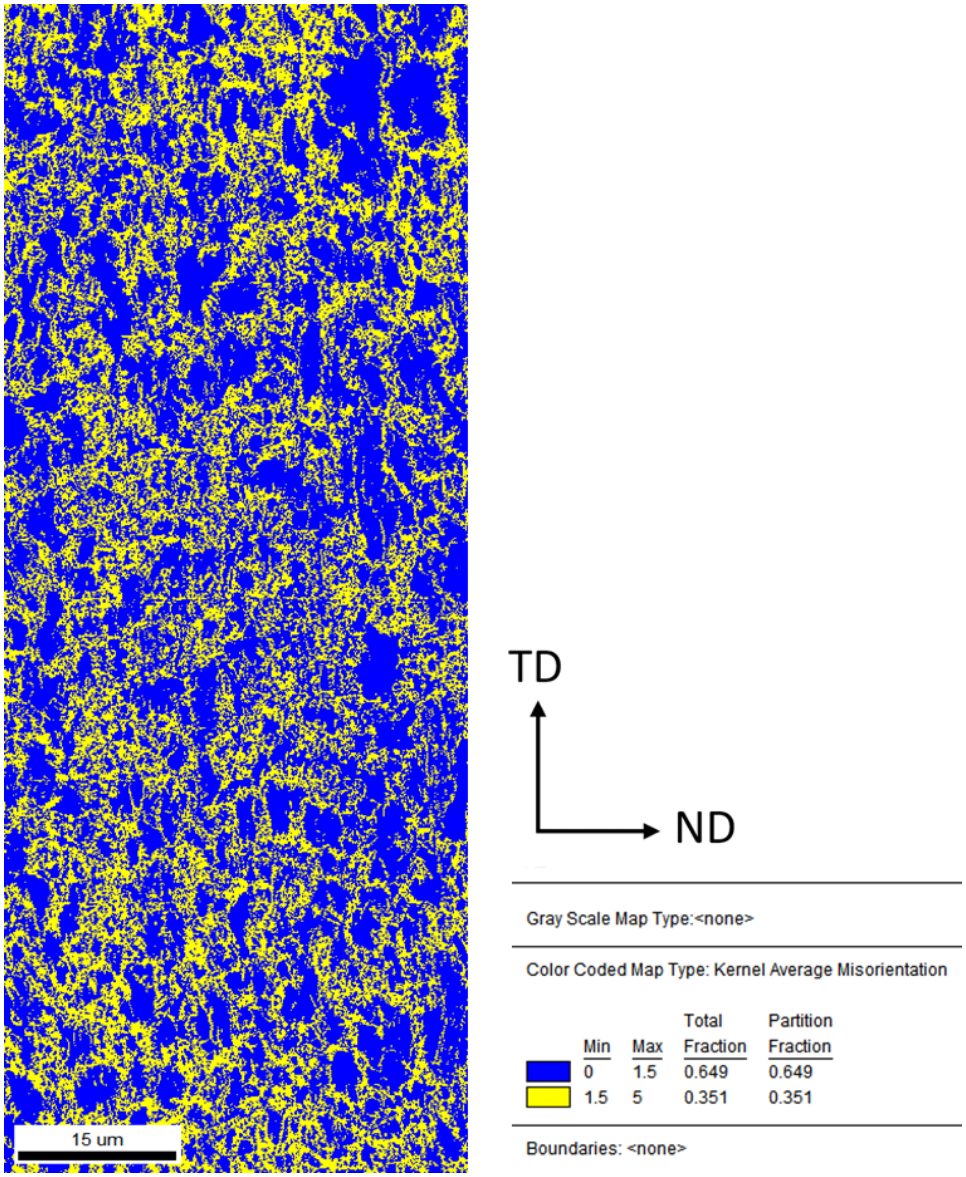

Fig. 5 Dichotomizing kernel-average misorientation (KAM) map of DP780 based on 1.5° KAM values

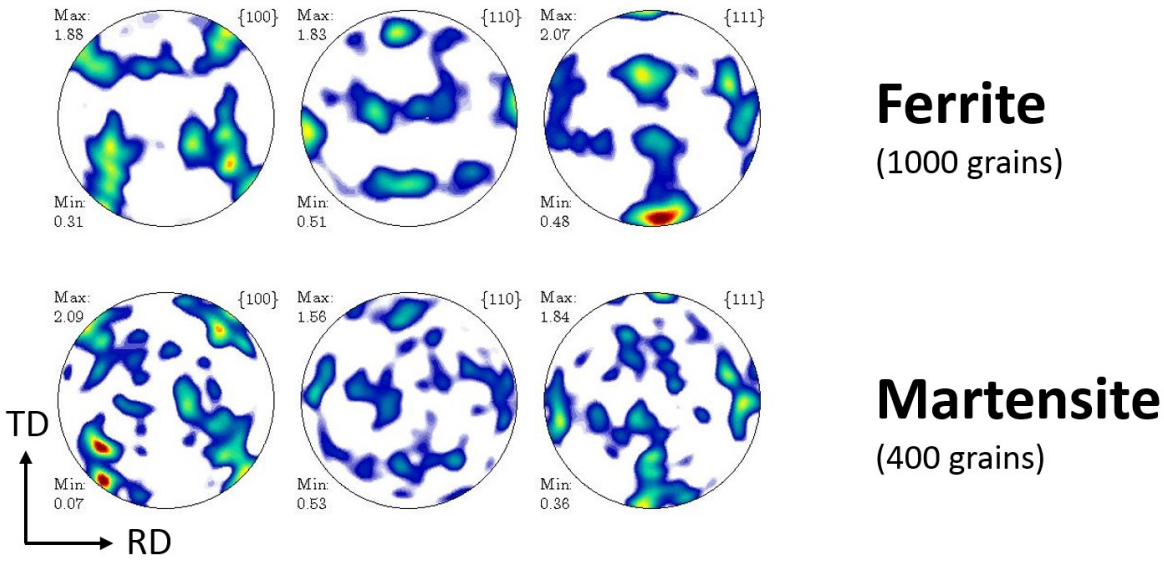

Fig. 6 (100), (110), and (111) pole figures associated with ferrite and martensite; these results are obtained by EBSD analysis

Using the EBSD data, the average grain sizes corresponding to ferrite and martensite of DP780 were estimated to be 4.14 μm and 3.04 μm, respectively. In the case of CHSP45R, optical microscopy was carried out to calculate the average grain size (6.75 μm).

3. Constitutive models

3.1 Micro-mechanical model (VPSC-RGBV)

In the VPSC-RGBV model, local plastic strain is related to local stress according to a visco-plastic power law:

$$\dot{\boldsymbol{\varepsilon}}^g = \dot{\gamma}_o \sum_s \mathbb{m}^s \left(\frac{\mathbb{m}^s : \boldsymbol{\sigma}^g}{\tau^s} \right)^n \qquad \text{Eq (2)}$$

where $\mathbb{m}^s$, $\dot{\gamma}_o$, n, $\boldsymbol{\sigma}^g$, and τ^s are the Schmid tensor, normalization rate factor, rate sensitivity exponent, local deviatoric stress tensor, and critical resolved shear stress (CRSS), respectively. The superscripts g and s denote that the associated quantities refer to a particular grain and slip system, respectively.

In the self-consistent crystal plasticity framework, the macroscopic response of the polycrystal is equivalent to the weighted average of local response over all the grains. Therefore, the macroscopic strain rate $\dot{\boldsymbol{E}}$ and stress $\boldsymbol{\Sigma}$ should follow $\dot{\boldsymbol{E}} = \sum_g \dot{\boldsymbol{\varepsilon}}^g f^g$ and $\boldsymbol{\Sigma} = \sum_g \boldsymbol{\sigma}^g f^g$, respectively, with f^g being the weight fraction of an individual grain.

The CRSS is determined by

$$\tau^s = \tau_d^s + \tau_B^s \qquad \text{Eq (3)}$$

where τ_d^s and τ_B^s denote contributions from the dislocation density and associated back-stress terms, respectively. The term τ_d^s is calculated using the extended Taylor law, which describes the latent hardening associated with interactions between dislocations (Kubin et al., 2008; Peeters et al., 2000, 2001a,b):

$$\tau_d^s = \tau_o^s + \mu b \sqrt{\sum_t \alpha^{st} \rho^t} \quad \text{Eq (4)}$$

where τ_o^s, μ, b, α, and ρ are the initial value of CRSS, shear modulus, magnitude of Burgers vector, hardening matrix, and total dislocation density, respectively. Both τ_d^s and τ_B^s are functions of two dislocation density terms, ρ_{for}^s and ρ_{rev}^s, which represent the forward and reversible dislocations, respectively (Kitayama et al., 2013). Each of the dislocation densities follows its distinctive evolution rule to approximate the formation and annihilation of dislocation structures during plastic deformation. The forward dislocation ρ_{for}^s quantifies the portion of the dislocation structure insensitive to the slip sense. On the other hand, the reversible dislocation ρ_{rev}^s represents those dislocations that may rearrange when the slip direction is switched, and thus is sensitive to the sense of slip. To denote reversible dislocations corresponding to the two separate shear senses, $+$ and $-$ symbols are used so that the total reversible dislocation density ρ_{rev}^s amounts to $\rho_{rev}^{s+} + \rho_{rev}^{s-}$.

The evolution of ρ_{for}^s and ρ_{rev}^s is based on the storage and recovery activities of the dislocation structure, which follows the classical Kocks-Mecking model (Mecking and Kocks, 1981). As in-depth descriptions of the evolution rule can be found elsewhere (Wen et al., 2016), only brief explanations are included here. Forward dislocation evolves according to the following rule:

$$d\rho_{for}^s = (1 - P^s) \frac{|d\gamma^s|}{b\Lambda} - f_R \rho_{for}^s d\Gamma \quad \text{Eq (5)}$$

where the factor P^s controls the fraction of reversible dislocations, f_R scales the fraction of dislocations subjected to thermal recovery, and Λ denotes the mean-free path. The mean-free path may evolve as a function of plastic activities through the relationship:

$$\frac{1}{\Lambda} = \frac{\sqrt{\rho}}{K} + \frac{1}{D} \quad \text{Eq (6)}$$

where ρ, D, and K are the total dislocation density of the grain, grain size, and the number of immobile dislocations that a moving dislocation segment will cut through before being immobilized by the obstacles, respectively. As mentioned earlier, as opposed to ρ_{for}^s, reversible dislocations are

sensitive to the slip shear sense and so is the evolution rule.

Case 1: When slip system s is active ($d\gamma^{s\pm} > 0$)

$$d\rho_{rev}^{s\pm} = P^s \frac{|d\gamma^s|}{b\Lambda} - f_R \rho_{rev}^{s\pm} d\Gamma \quad \text{Eq (7)}$$

$$d\rho_{rev}^{s\mp} = -\frac{1}{b\Lambda}\left(\frac{\rho_{rev}^{s\mp}}{\rho_o^s}\right)^m |d\gamma^s| \quad \text{Eq (8)}$$

Case 2: When slip system s is inactive ($d\gamma^{s\pm} = 0$)

$$d\rho_{for}^{s} = -f_R \rho_{for}^{s} d\Gamma \quad \text{Eq (9)}$$

$$d\rho_{rev}^{s\pm} = -f_R \rho_{rev}^{s\pm} d\Gamma \quad \text{Eq (10)}$$

In the following discussion, the superscripts $s\pm$ and $s\mp$ are used such that the $s+$ and $s-$ signs alternate for the given shear sense of a slip system s. For instance, when $+$ slip sense occurs, $d\rho_{rev}^{s+}$ follows Eq (7), whereas $d\rho_{rev}^{s-}$ follows Eq (8). ρ_o^s in Eq (8) is the snapshot value of the total dislocation density saved at the last instant when the slip shear sense was reversed. The power law form, i.e., $\left(\frac{\rho_{rev}^{s\mp}}{\rho_o^s}\right)^m$ with exponent m introduced in Eq. (8), captures the high rate of recombination of reversible dislocations.

The back-stress term τ_B^s in Eq. (3) follows an empirical power law proposed by Wen et al. (2016)

$$\tau_B^s = -\tau_d^s f_B^s \left(\frac{\rho_{rev}^{s\mp}}{\rho^s}\right)^q \quad if \quad d\gamma^{s\pm} > 0 \quad \text{Eq (11)}$$

where f_B^s $(0 < f_B^s \leq 1)$ is a factor that scales the coupling effect between reversible dislocation and back-stress. Note that the opposite $\mp$ sign is relevant for the associated reversible dislocation, as opposed to the active slip sense of the shear increment $d\gamma^{s\pm}$. The exponent q controls the rate, at which the back-stress diminishes as the reversible dislocation pertaining to the opposite shear sense decreases.

3.2 Macro-mechanical model (HAH-Yld2000-2d)

In this section, the homogeneous anisotropic hardening (HAH) model for distortional plasticity is briefly described. In the HAH model, the yield function is described using the following equation:

$$\Phi(\boldsymbol{\Sigma}) = \left[\phi^{\mathrm{a}}(\boldsymbol{\Sigma}) + f_1^a \left|\hat{\mathbf{h}}:\boldsymbol{\Sigma} - \left|\hat{\mathbf{h}}:\boldsymbol{\Sigma}\right|\right|^{\mathrm{a}} + f_2^a \left|\hat{\mathbf{h}}:\boldsymbol{\Sigma} + \left|\hat{\mathbf{h}}:\boldsymbol{\Sigma}\right|\right|^{\mathrm{a}}\right]^{\frac{1}{\mathrm{a}}} = \bar{\Sigma} \quad \text{Eq (12)}$$

where $\boldsymbol{\Sigma}$ is the macro stress deviator and a is a constant exponent; ϕ denotes the so-called stable component, a homogeneous anisotropic yield function; $\hat{\boldsymbol{h}}$ is the normalized microstructure deviator that accounts for microstructure evolution during deformation; f_1 and f_2 are state variables that scale the degree of distortion due to the Bauschinger effect. Four material parameters g_i (i = 1–4) and the state variables k and k_i (i = 1–5) are required to describe the evolution of $\hat{\boldsymbol{h}}$. g_1 and g_2 influence the evolution of f_1 and f_2, respectively, through $f_i = (\frac{1}{g_i} - 1)^{\frac{1}{a}}$ (i = 1, 2), whereas g_3 and g_4 affect permanent softening. The nonquadratic anisotropic yield function, Yld2000-2d (Barlat et al., 2003b), was selected as the stable component ϕ in this work; it requires eight anisotropy coefficients α_i (i = 1–8), which are usually characterized through three uniaxial tension tests and a biaxial tension test.

4. Model calibration

In this section, the VPSC-RGBV and HAH models are used to characterize the two chosen materials. In our previous study (Zaman et al., 2017), the constitutive parameters of the HAH model were identified for both CHSP45R and DP780 using all the mechanical experiments discussed in Section 2.2. In contrast, the VPSC-RGBV model requires only a limited number of experiments, which are conducted in the current investigation. This is to check the idea that an exhaustive set of experiments required for HAH model identification can be assisted by the use of the VPSC-RGBV model.

4.1 VPSC-RGBV model characterization

The initial crystallographic texture was analyzed using the XRD and EBSD methods – the XRD analysis was sufficient for CHSP45R, whereas both the XRD and EBSD scans were needed for DP780. A population of 1000 discrete orientations was selected to represent the body-centered cubic (BCC) phase in CHSP45R. In contrast, two separate sets of populations were created for DP780 – 1) 1000 discrete orientations; the two halves of this population represent ferrite and martensite textures, but they are based on the same averaged texture obtained using XRD and 2) a population consisting of 1000 ferritic orientations and 400 martensitic orientations that were separately obtained using the EBSD data with KAM analysis as explained in Section 2.3. Note that a ferrite-to-martensite phase ratio of 65:35 was used.

The constitutive parameters related to the evolution of dislocation densities were identified using the Simplex algorithm as implemented in the SciPy package of Python (Nelder and Mead, 1965). An objective function χ that quantifies the difference between an experimental stress-strain curve and its predicted counterpart was used.

$$\chi = \frac{\sqrt{\sum_{i=1}^{n}(\sigma_i{}^{VPSC} - \sigma_i{}^{EXP})^2}}{n-1} \qquad \text{Eq (13)}$$

Here, $\sigma_i{}^{VPSC}$ and $\sigma_i{}^{EXP}$ denote the flow stresses obtained at given strains from the VPSC-RGBV simulation and experiment, respectively. The individual stress data were sampled at 100 different levels of strain (i.e., $n = 100$). The repeated evaluation of χ value halts when a given tolerance or the maximum iteration number is reached.

Table 2 shows the VPSC-RGBV model parameters and the method by which they were determined. Because the elastic shear modulus and Burgers vector are similar for ferritic steels, the values that were used in a previous work (Wen et al., 2016) were selected. The effect of the recombination rate parameter, m in Eq. (8), was not optimized as it was observed that the effect of m was negligible for the current study. Instead, a value of $m = 0.5$ was selected for the calculation, as suggested by Wen et al. (2016). The grain size was determined from experimental measurements as

explained in Section 2.3. Therefore, the coefficients, τ_o^s, K, f_R, α^{st}, f_B^s, and q were chosen as the arguments of χ in Eq. (13). In the case of the hardening matrix α, only the latent hardening coefficient (i.e., the off-diagonal components of α^{st} with $s \neq t$) was subjected to parameter identification, whereas the self-hardening coefficient (i.e., with $s = t$) was fixed as 1. In addition, in a BCC crystal structure, potentially active slip systems are generally assumed to belong to one of the two families, {110} <111> or {112} <111>. Polycrystals are deformed by imposing a strain rate tensor normalized to $10^{-3}/s$ over the course of a given loading scenario, which corresponds to the strain rate imposed in the experimental work.

The stress-strain curve resulting from the TDT-TDC experiment was used to calculate σ_i^{EXP} in Eq. (13) for VPSC-RGBV model characterization. Tables 3 and 4 list the VPSC-RGBV parameters characterized for CHSP45R and DP780, respectively.

Table 2 Parameters of the VPSC model and their determination methods

Model parameters	Determination method
μ: Shear modulus b: Burgers vector m: Recombination rate parameter	Reference paper (Wen et al., 2016)
D: Grain size	OM or EBSD (Section 2.3)
τ_o: Initial CRSS K: Mobile to storage parameter f_R: Recovery parameter α^{st}: Latent hardening coefficient f_B^S: Back-stress parameter q: Back-stress exponent	Simplex optimization

Table 3 VPSC-RGBV model parameters for the CHSP45R steel sheet

Model parameters	Values
τ_o: Initial CRSS	113 MPa
K: Mobile to storage parameter	980
f_R: Recovery parameter	5.0
α^{st} : Latent hardening coefficient	0.05
f_B^S: Back-stress parameter	0.41
q: Back-stress exponent	3.00

Table 4 VPSC-RGBV model parameters for the DP780 steel sheet

Model parameters	Single phase	Dual phase	
		Ferrite	Martensite
τ_o: Initial CRSS	226 MPa	150 MPa	600 MPa
K: Mobile to storage parameter	70	53	12
f_R: Recovery parameter	4.89	6.40	0.01
α^{st}: Latent hardening coefficient	0.009	0.024	0.001
f_B^S: Back-stress parameter	0.75	0.78	0.98
q: Back-stress exponent	2.26	1.55	2.00

4.2 HAH model characterization

The constitutive parameters of the HAH model used by Zaman et al. (2017) were used in the current study. The HAH model was identified by considering the best approximation of the experimental observations including 1) the in-plane variation of flow stresses and r-values from three uniaxial tension tests conducted on the as-received sample, 2) yield loci evolution from TDT-BT tests, and 3) the evolution of the stress-strain and r-value curves in TDT-RDT and TDT-DDT tests.

More specifically, the reverse loading coefficients (k_i with i = 1–5) were manually determined from the flow stress curves obtained from TDT-RDT. The other coefficients, including the microstructure deviator rotation rate (k) and cross-loading coefficients ($k_L, L, k_s, k_{s'}$ and S) were obtained from the best approximation of the TDT-DDT flow curve and yield locus after pre-strain. The material coefficients for Yld2000-2d, the Swift hardening law, and HAH model are listed in Table 5.

Table 5. HAH-Yld2000-2d coefficients (Zaman et al., 2017)

(1) Swift isotropic hardening ($\sigma = A(\varepsilon_o + \bar{\varepsilon})^n$)		
A	ε_o	n
CHSP45R		
733	6.5×10^{-3}	0.167
DP780		
1315	5.0×10^{-5}	0.141

(2) Yld2000-2d							
α_1	α_2	α_3	α_4	α_5	α_6	α_7	α_8
CHSP45R							
1.094	0.894	0.806	1.976	0.984	0.908	1.042	1.085
DP780							
0.955	0.960	1.006	0.991	1.014	0.983	1.006	1.035

(3) HAH model with $a = 2$									
k	k_1	k_2	k_3	k_4	k_5	k_L	L	S	$k_s, k_{s'}$
CHSP45R									
35	250	6.0	0.45	0.95	15	70	5.6	0.50	7.0
DP780									
140	130	20	0.47	0.94	8.0	•	1.0	0.46	8.0

• The coefficient k_L does not influence the results in this case, as L is equal to 1.

5. Results

The VPSC-RGBV model does not account for elasticity and thus is not able to capture elastic effects. To facilitate direct comparison with the simulation results, the elastic strain was eliminated from all the experimental data. It should also be noted that the VPSC-RGBV results of DP780 are

based on two different sets of discrete orientations – 1) one based on the deconvoluted XRD pole figures by assuming that DP780 exists as a single-phase BCC structure (denoted hereinafter as VPSC-SPH) and 2) another using two separate populations of orientations pertaining to ferrite and martensite; these orientations are obtained by the EBSD KAM analysis (denoted hereinafter as VPSC-DPH) – see Section 2.3 for more details.

In what follows, the TDT-TDC experimental result is compared with the calibrated VPSC-RGBV model. Afterwards, the predictive capability of VPSC-RGBV is evaluated with respect to HAH-Yld2000-2d in terms of various experimental results, including the 1) stress-strain curves from TDT-DDT and TDT-RDT, 2) instantaneous r-value after strain-path change, and 3) yield surface evolution.

5.1 VPSC-RGBV calibration for load reversal

Fig. 7 shows the experimental stress-strain curves of TDT-TDC and the fitting of VPSC-RGBV model together with the monotonic TDT for CHSP45R. The TDT-TDC flow curve exhibits the Bauschinger effect upon load reversal, which is followed by a high hardening rate within a strain range of about 2% and a saturation at a lower stress than that of the monotonic TDT (i.e., permanent softening). Qualitatively, all these features were well captured by the fitted result of the VPSC-RGBV model. Yet, the flow stress after load reversal was slightly over-estimated. During the VPSC-RGBV model calibration, the maximum number of iterations was reached, while χ in Eq. (13) saturated to a value larger than the given tolerance. Numerical optimization was performed with a few different sets of initial estimates, but the discrepancy in the compressive loading sequence of the TDT-TDC curve was persistent. Hence, it is believed that the discrepancy is primarily due to the prediction accuracy of the model itself.

In Fig 8. the evolution of texture obtained from the VPSC-RGVB model is shown at three different states: a) as-received, b) 6% TD tension, and c) TDT-TDC sequential loading. As evident in the figure, the evolution in crystallographic texture is not significant. Therefore, the effect of texture evolution on the flow stress behavior is assumed negligible in the current study.

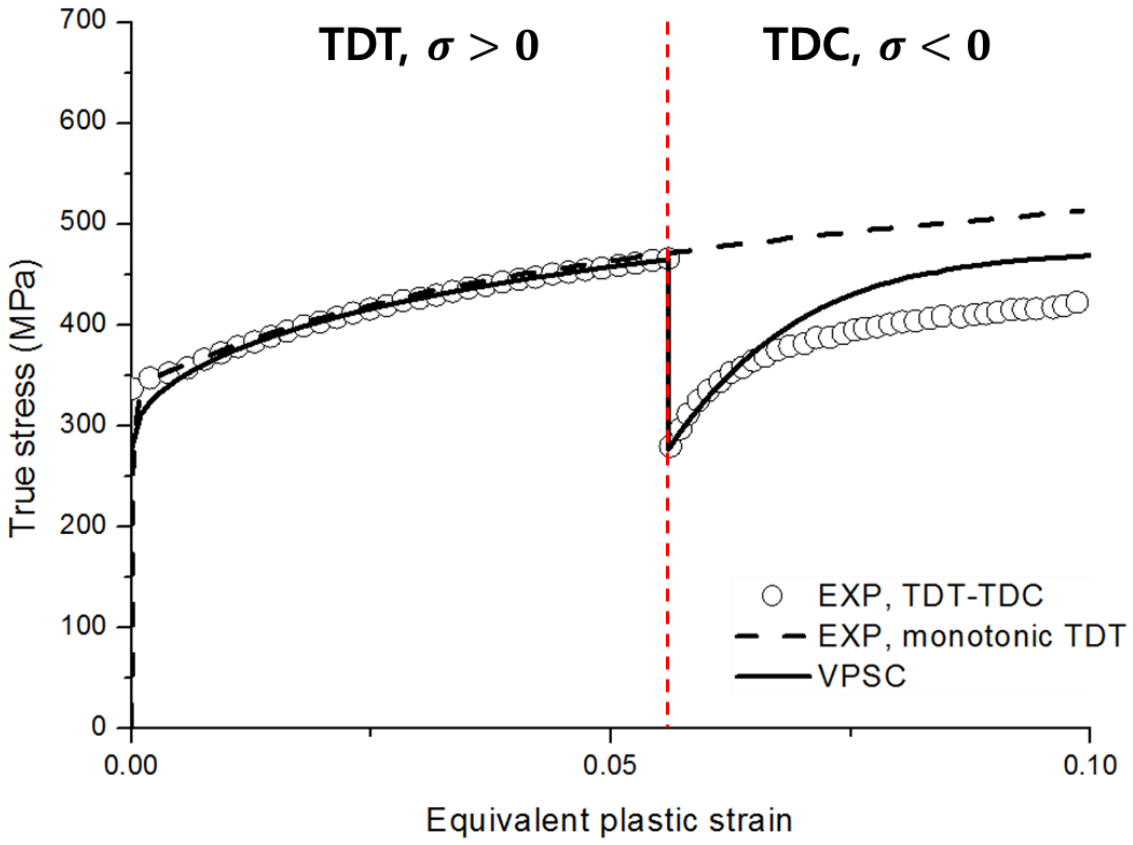

Fig. 7 Experimental tension-compression and monotonic stress-strain curves of CHSP45R with VPSC-RGBV model prediction

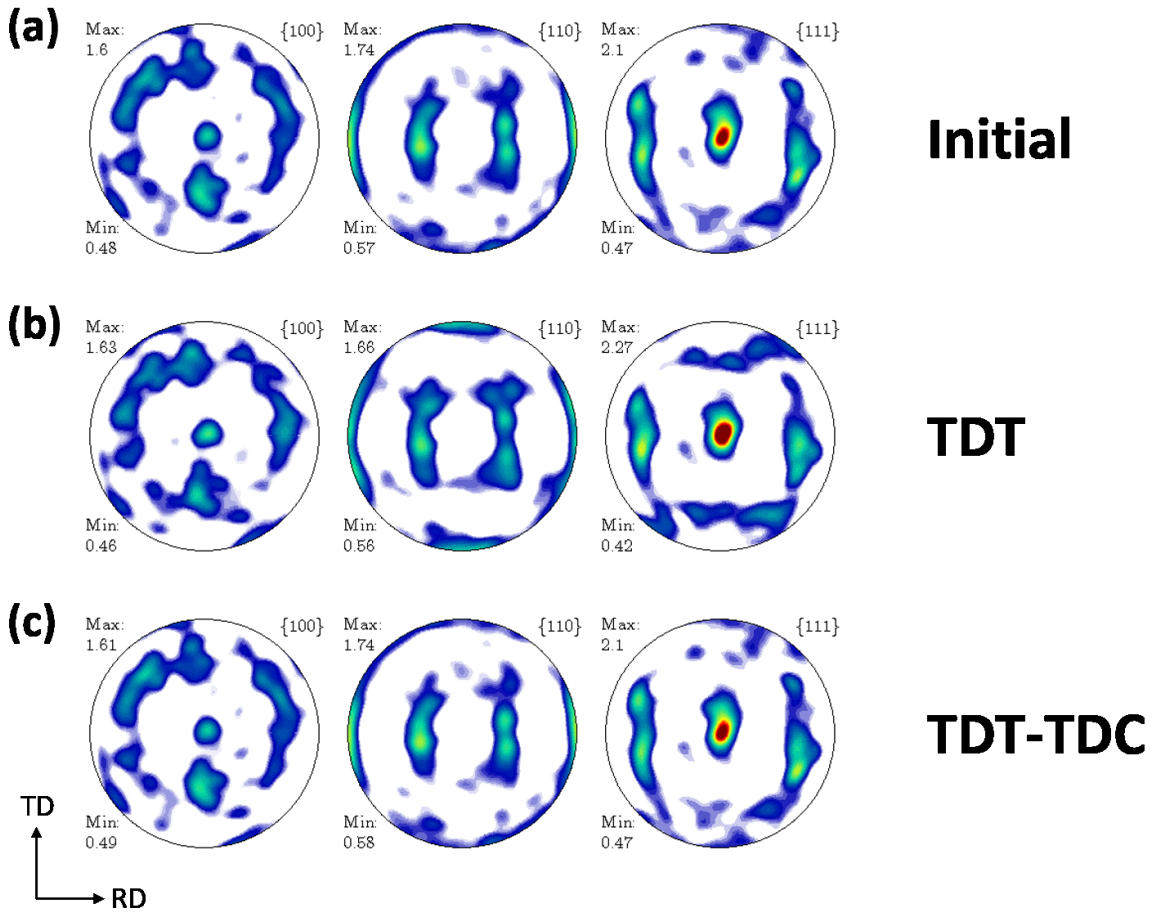

Fig. 8 Predicted crystallographic texture (a) initial state and (b) after 6% TD tension pre-strain (c) followed by 5% TD compression.

The same calibration method was applied to DP780 and the results are shown in Fig. 9. Similar to CHSP45R, both the Bauschinger effect and permanent softening were observed. Overall, the fit of the stress-strain curve with VPSC-DPH was in better agreement with the experimental results than that of VPSC-SPH. Similar to CHSP45R, discrepancy in the TDT loading sequence of VPSC-SPH fitting recurred with several different sets of initial estimates.

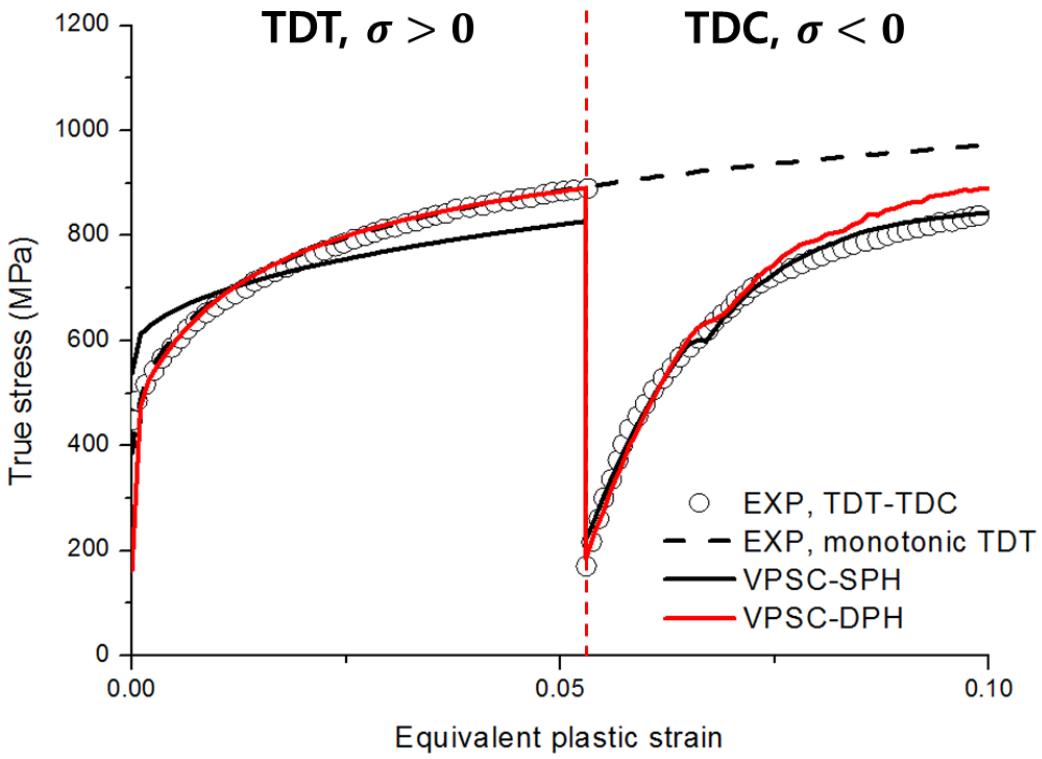

Fig. 9 Experimental tension-compression and monotonic stress-strain curves of DP780 with two different types of VPSC-RGBV model prediction

5.2 Stress-strain curves involving cross-loading

Fig. 10 shows the experimental stress-strain curves of CHSP45R resulting from the TDT-RDT and TDT-DDT loading sequences together with the model calculations based on VPSC-RGBV and HAH. In the case of TDT-RDT (Fig. 10a), the VPSC-RGBV model roughly predicted the trend of the experimental behavior and the Bauschinger effect and latent hardening were qualitatively captured. However, the slight stress overshooting shown in the TDT-DDT (Fig. 10b) experiment could not be captured by the VPSC-RGBV model. The HAH-Yld2000-2d model captured both TDT-RDT and TDT-DDT flow stress curves reasonably well. Fig. 11 shows the results of DP780 steel using the same loading sequences as in Fig. 10. The results indicate that VPSC-DPH results are in much better agreement with the experimental results with both loading conditions in comparison to VPSC-SPH. In the case of the HAH model, both sets of experimental stress-strain curves were well captured.

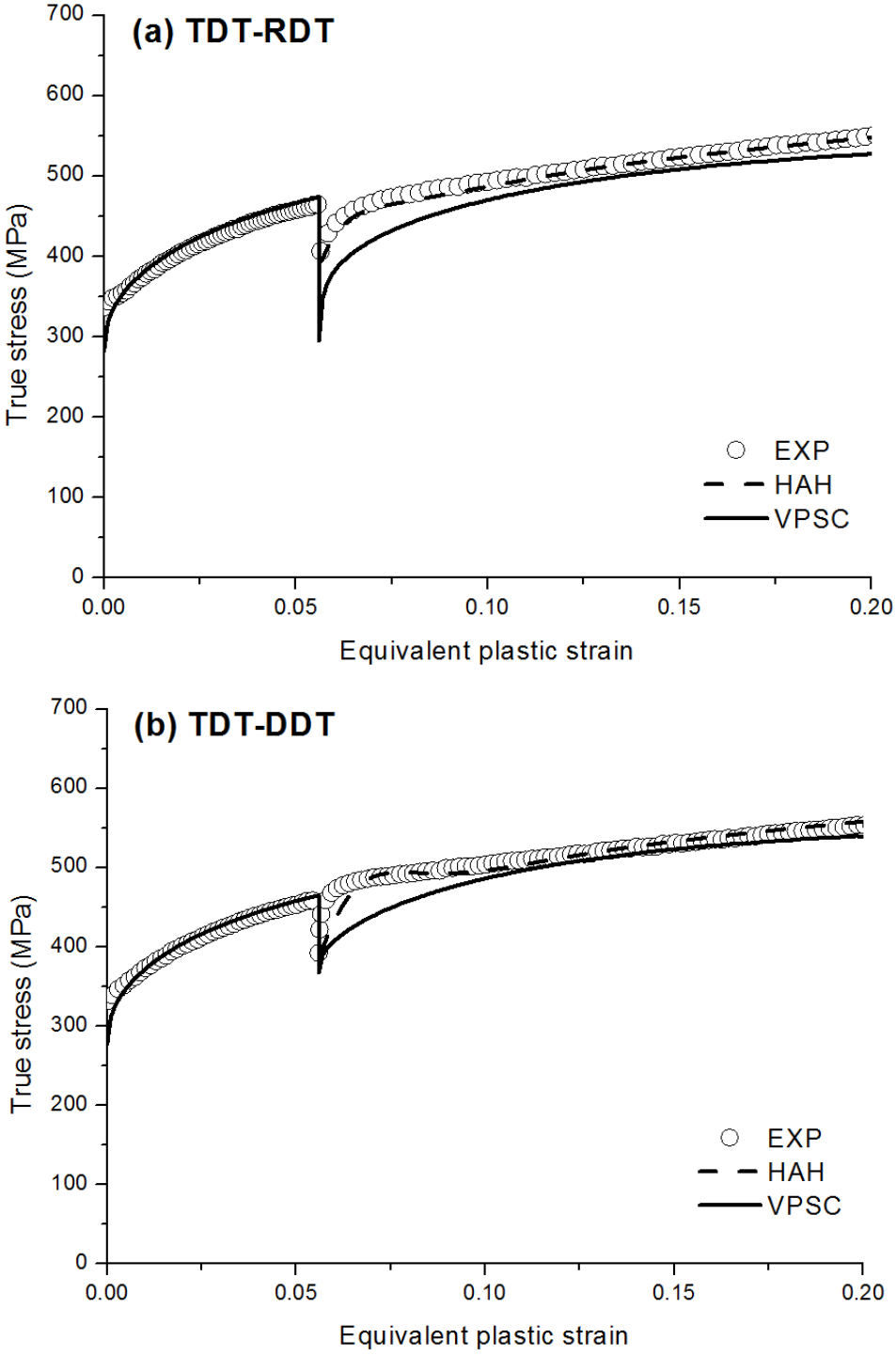

Fig. 10 Experimental and predicted VPSC and HAH of CHSP45R stress-strain curves with strain-path changes at (a) 90° and (b) 45° from the pre-strain direction, TD

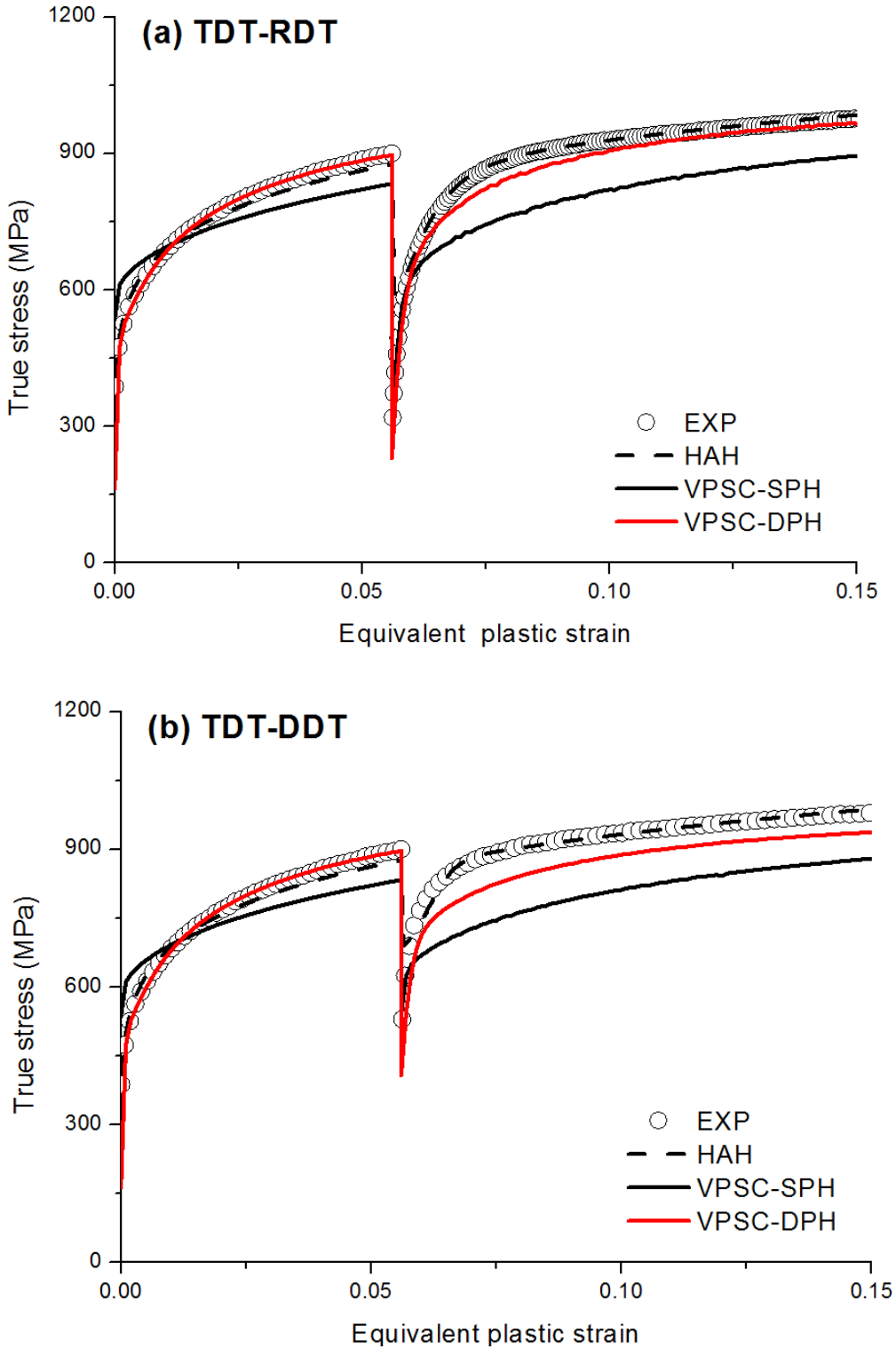

Fig. 11 Experimental and predicted VPSC and HAH of DP780 stress-strain curve with strain-path changes at (a) 90° and (b) 45° from the pre-strain direction, TD

5.3 R-value evolution after strain-path change

Figs. 12 and 13 illustrate the evolution of the r-value determined from the TDT-RDT and TDT-DDT sequences, respectively, for CHP45R and DP780. Both figures show the change of r-value according to given path changes after prestrain of uniaxial tension 6 % (engineering strain) in TD direction. In the case of CHSP45R (Fig. 12), the VPSC-RGBV predictions are in good agreement with the experiments; in particular, both the initial fluctuation and the saturation of the r-value were well captured for TDT-RDT. Moreover, the trend was captured for TDT-DDT as well. In contrast, the accuracy of the HAH model was rather poor.

In the case of DP780 (Fig. 13), the predictions of the VPSC-RGBV and HAH models were in better agreement with the experiments. The HAH model captured the drastic initial changes in the r-values in both loading sequences as shown in Figs. 13a and 13b. Both the VPSC-RGBV predictions (VPSC-SPH and VPSC-DPH) are in very good agreement with the experimental results in the case of TDT-RDT. Although the VPSC-RGBV prediction for TDT-DDT did not show the initial upsurge, the saturation value was captured.

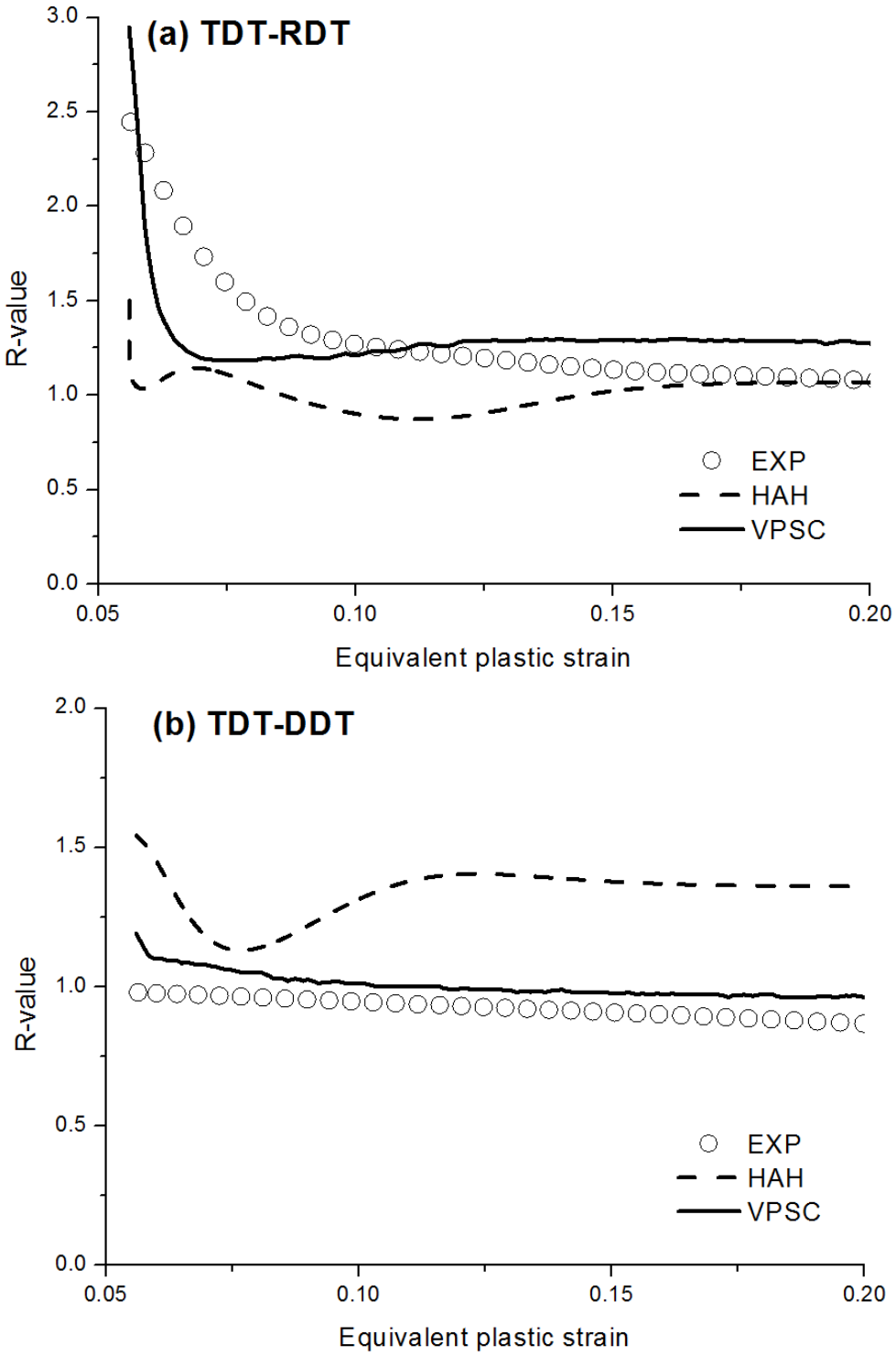

Fig. 12 Experimental and predicted VPSC and HAH of CHSP45R r-value evolution after strain-path changes at (a) 90° and (b) 45° from the pre-strain direction TD

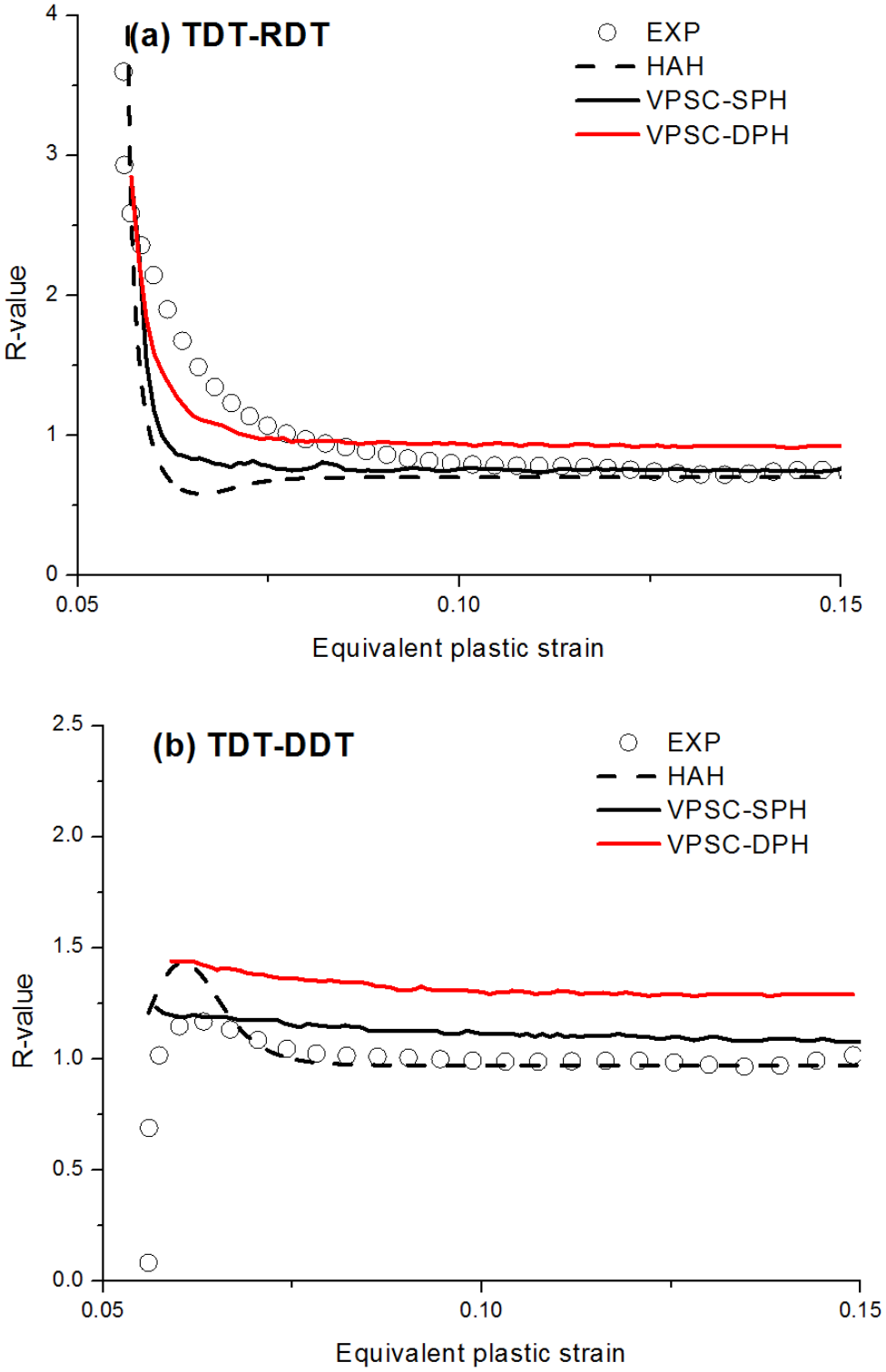

Fig. 13 Experimental and predicted VPSC and HAH of DP780 r-value evolution after strain-path changes at (a) 90° and (b) 45° from the pre-strain direction TD

5.4 Yield surface evolution

Figs. 14 and 15 show the yield locus evolution of CHSP45R and DP780, respectively, resulting from the TDT-BT and BT experiments with three separate stress ratios (1:2, 1:1, and 2:1) together with the TDT-TDC, TDT-RDT and the monotonic uniaxial tension experiments. The stress coordinates on the yield locus were normalized by the uniaxial tension along the TD in order to better visualize shape changes. In these figures, two separate types of yield locus are displayed – 1) the initial yield locus corresponding to the as-received sample (denoted by the black lines or symbols) and 2) subsequent yield locus obtained after TDT loading with 6% strain (denoted by red lines or symbols) and reloaded in biaxial tension. For the experimental determination of the yield surface, the stress values corresponding to a fixed amount of plastic work, equivalent to about 0.2% strain offset, were considered. The same method was applied for the model-predicted yield loci. Note that a subsequent yield locus strongly depends on the amount of the offset strain. The yield locus changes at various offset strains were demonstrated in previous study, Jeong et al. (2017).

Fig. 14 shows that both the VPSC-RGBV and HAH-Yld2000-2d models led to good agreement with the initial experimental yield surface shape of CHSP45R. In the case of the yield surface obtained after TDT prestrain (red), the HAH model led to a slightly better agreement with the experimental results compared to VPSC-RGBV for the three biaxial loading paths and the RDT sequence, whereas the prediction by VPSC-RGBV led to much better agreement with the experimental results compared to HAH model calculation for the TD compressive yield stress upon load reversal.

In the case of DP780, as shown in Fig. 15, the results of the HAH model at both the initial condition and TD 6% are in good agreement with the experiments. The predictions obtained with the VPSC-RGBV model are also in good agreement with the experimental results. Particularly, after TDT prestrain, VPSC-DPH led to a somewhat better prediction in comparison to VPSC-SPH for the biaxial states.

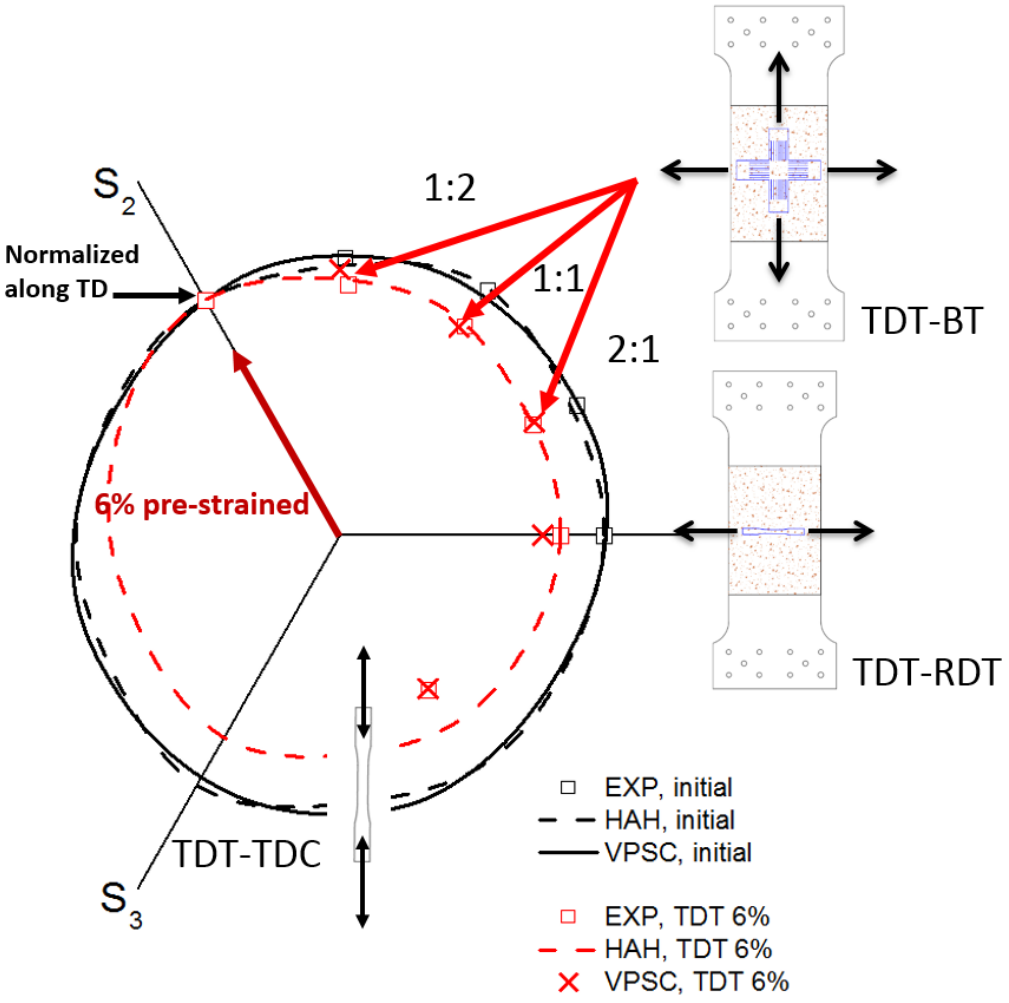

Fig. 14 Experimental and predicted VPSC and HAH of CHSP45R yield surface before and after 6% uniaxial TD pre-strain in the **π**-plane

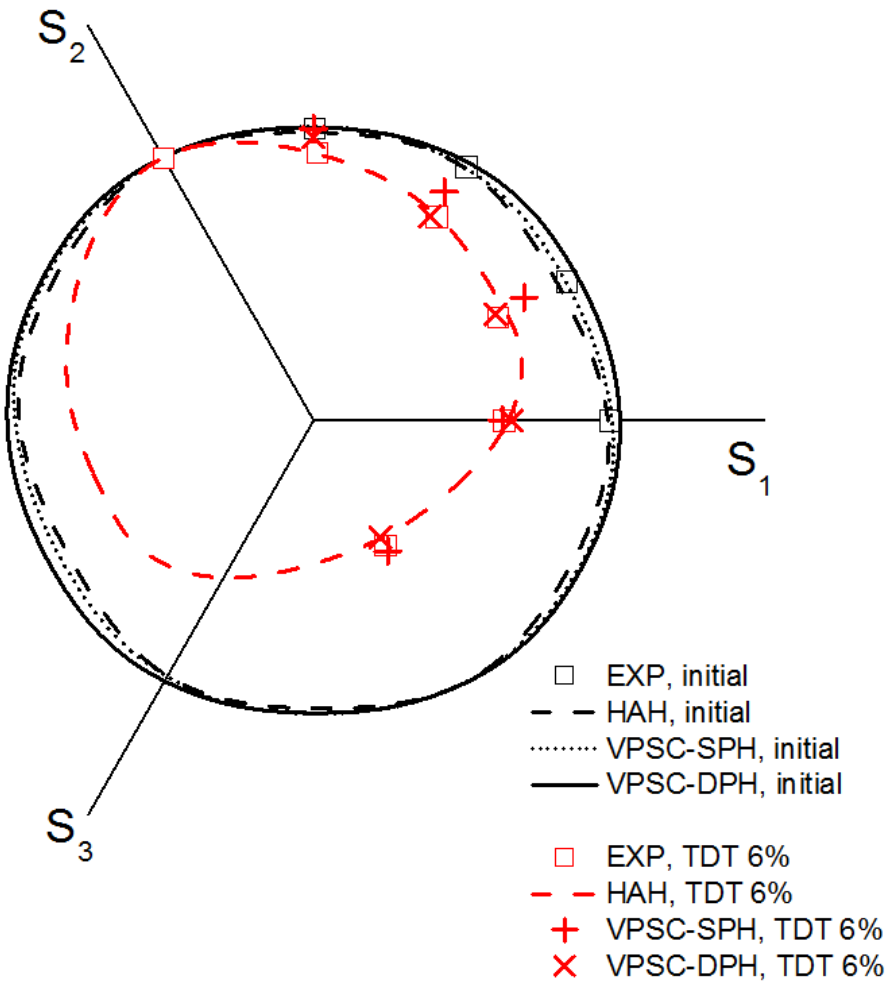

Fig. 15 Experimental and predicted VPSC and HAH of DP780 yield surface before and after 6% uniaxial TD pre-strain in the **π**-plane

6. Discussion

6.1 Optimized material parameters of DP steel

The constitutive parameters associated with dislocation hardening model employed in VPSC-RGBV are closely linked to microstructural features. However, microscopic parameters are very difficult to be determined experimentally. The main goal of the current study is to develop a methodology, where the VPSC-RGBV model can assist the experimental characterization of the HAH model. Therefore, it is inappropriate to conduct micro-scale experiments to directly obtain the constitutive parameters. Instead, the parameter calibration presented in this study solely relied on the numerical optimization procedure, as discussed in Section 4.1. In this case, special care should be paid to the numerical optimization procedure as it may lead to unrealistic values. To at least eliminate obviously invalid solutions, a series of parametric studies on each material parameter was conducted in Kim (2018), which demonstrated the effects of individual parameters on the macroscopic loading behavior.

The case of DP780 needs a thorough examination as the number of constitutive parameters is significantly higher in comparison to previous studies on single-phase alloys (Jeong et al., 2016; Kitayama et al., 2013; Wen et al., 2016). Therefore, each individual parameter of DP780 in Table 4 is examined in the following discussion.

For single-phase alloys, the initial CRSS τ_o^s can be roughly estimated using the uniaxial yield stress and Taylor factor. However, for DP780, martensite should be 3 to 4 times harder than ferrite (Al-Abbasi and Nemes, 2003; Ha et al., 2017; Kim et al., 2012). Indeed, the calibrated τ_o^s value of martensitic phase (600 MPa) is approximately 4 times higher than that of ferrite (150 MPa).

The value of K for martensite is lower than that for ferrite. Assuming that the grain size D and amount of total dislocations ρ are fixed, Eq. (6) indicates that the mean free path Λ can be expressed as a function of K alone. In that case, the mean free path increases as the number of immobile dislocations crossed by a moving segment increases. Fig. 16 shows such a relationship

using the average dislocation densities (i.e., $4 \times 10^{13}/m^2$ for ferrite and $2 \times 10^{14}/m^2$ for martensite), resulting from separately conducted VPSC-RGBV simulations using single-phase ferrite and martensite polycrystals. Huang et al. (2016) obtained a quantitative relationship between the dislocation density and mean free path for DP800 steel with grain size and phase fraction similar to that of DP780 used in this work. Using their equation, the mean free paths corresponding to the aforementioned dislocation densities were calculated to be 2.8×10^{-6} m and 6×10^{-7} m for ferrite and martensite, respectively, which indicates the mean free path of ferrite is approximately 5 times larger than that of martensite. A similar value can be observed in Fig. 16, when $K \approx 55$ for ferrite (point A) and $K \approx 10$ for martensite (point B). This indicates that K, as determined in this work, is consistent with values extracted from literature. In addition, Bergström et al. (2010) found that the mean free path decreases as the volume fraction of martensite in DP steel increases, which suggests that K (and thus the mean free path) should be lower in martensite than in ferrite.

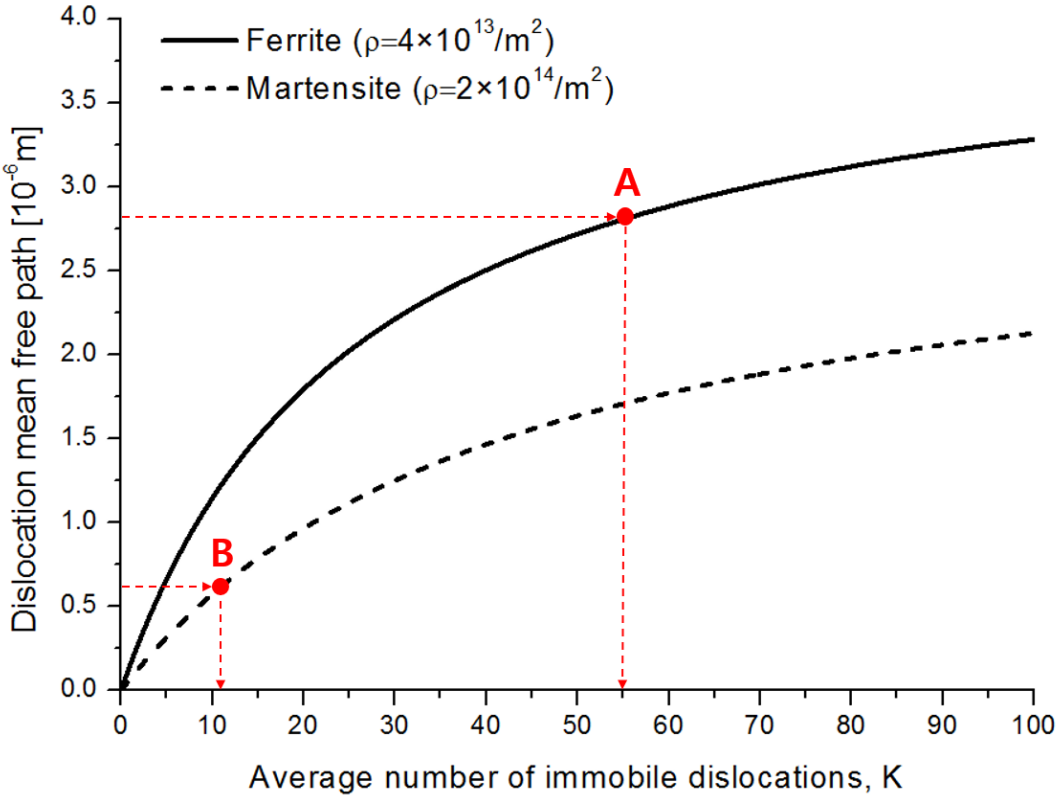

Fig. 16 Evolution of dislocation mean free path according to $\boldsymbol{K}$ value for a fixed value of grain size and dislocation density. Two separate dislocation densities ($\mathbf{4 \times 10^{13}}$ $\boldsymbol{/m^2}$ for ferrite and $\mathbf{2 \times 10^{14}}$ $\boldsymbol{/m^2}$ for marteniste) were plotted.

In the case of the thermal recovery parameter f_R, the value corresponding to martensite is smaller than that for ferrite. As f_R increases, the effect of thermally activated recombination is enhanced, thus reducing the hardening rate. Similar results are found in the literature. For instance, Ghassemi-Armaki et al. (2014) conducted micropillar compression tests separately on ferritic and martensitic regions of a dual-phase steel sample, which indicates that the hardening rate of martensite is higher than that of ferrite. According to similar VPSC simulations conducted by Cong et al. (2009), a martensitic phase exhibits a higher strain hardening rate than ferrite.

An increase in either the latent or self-hardening coefficients generally enhances the strain hardening effect. The optimization procedure conducted in this study led to a latent hardening coefficient of 0.05 for single-phase CHSP45R. The latent hardening coefficient of DP780 was estimated to be as low as 0.009, based on the single-phase approximation (VPSC-SPH). VPSC-DPH resulted in quite dissimilar values for martensite and ferrite – 0.001 for martensite and 0.024 for ferrite. It should be mentioned here that optimization with a fixed latent hardening coefficient for DP780 led to a poorer predictive accuracy (not shown in this study). Therefore, it is believed that such a trend is required to improve the accuracy of the model. To validate the latent hardening parameters in use, experimental verification is required.

The parameter f_B^S controls the amount of back-stress and adjusts the Bauschinger ratio, which is defined as $(\sigma_f - \sigma_r)/2\sigma_f$, where σ_f and σ_r denote the stresses in the forward and reverse loading at reversal, respectively. Higher the f_B^S, lower is the re-yielding stress, which decreases the Bauschinger ratio in the VPSC-RGBV model. According to Kim et al. (2012) and Weiss et al. (2015), at a higher martensite fraction in DP steel, a lower Bauschinger ratio is obtained, which suggests that the increase in the Bauschinger effect can be attributed to the presence of martensite. Therefore, it is reasonable to obtain a higher value of f_B^S for martensite than ferrite.

So far, in this discussion, we qualitatively confirmed the validity of the constitutive parameters pertaining to martensite and ferrite in DP780. In what follows, this validity is further investigated by examining the respective mechanical responses of individual phases under the TDT-TDC loading

sequence. To this end, two additional VPSC-RGBV simulations were conducted using single-phase ferrite and single-phase martensite polycrystalline aggregates obtained by the EBSD-KAM analysis presented in Section 2.3. The results of these additional simulations are summarized in Fig. 17, which contains 1) the stress-strain curves calculated from the single-phase assumption, 2) phase-specific stress-strain curves of VPSC-DPH, and 3) the overall and experimental stress-strain curves from Fig. 9.

The phase specific stress-strain curves (dashed lines) are almost identical to those found in other reports (Al-Abbasi and Nemes, 2003; Ha et al., 2017; Kim et al., 2012), which suggests that the load-partitioning depicted in VPSC-DPH is reasonable. Fig. 17 shows that the *composite effect* is evident; the flow stress of martensite calculated by VPSC-DPH (blue bold line) is much lower than that obtained from single-phase martensite (blue dashed line). This composite effect is mainly attributed to the constraint between the mild ferrite and hard martensite. In addition, the strain rate difference might play a significant role as a material is considered to be visco-plastic in the VPSC-RGBV model. Accordingly, Fig. 18 implies that soft ferrite deforms up to a much higher strain than the hard martensite, when a dual-phase polycrystal is subjected to loading. Therefore, the martensite considered in VPSC-DPH is exposed to a much lower strain rate than that in the case of a single-phase simulation. The strain rate of ferrite is not significantly influenced by the presence of martensite and the flow stress levels in both cases are almost identical (Fig. 17).

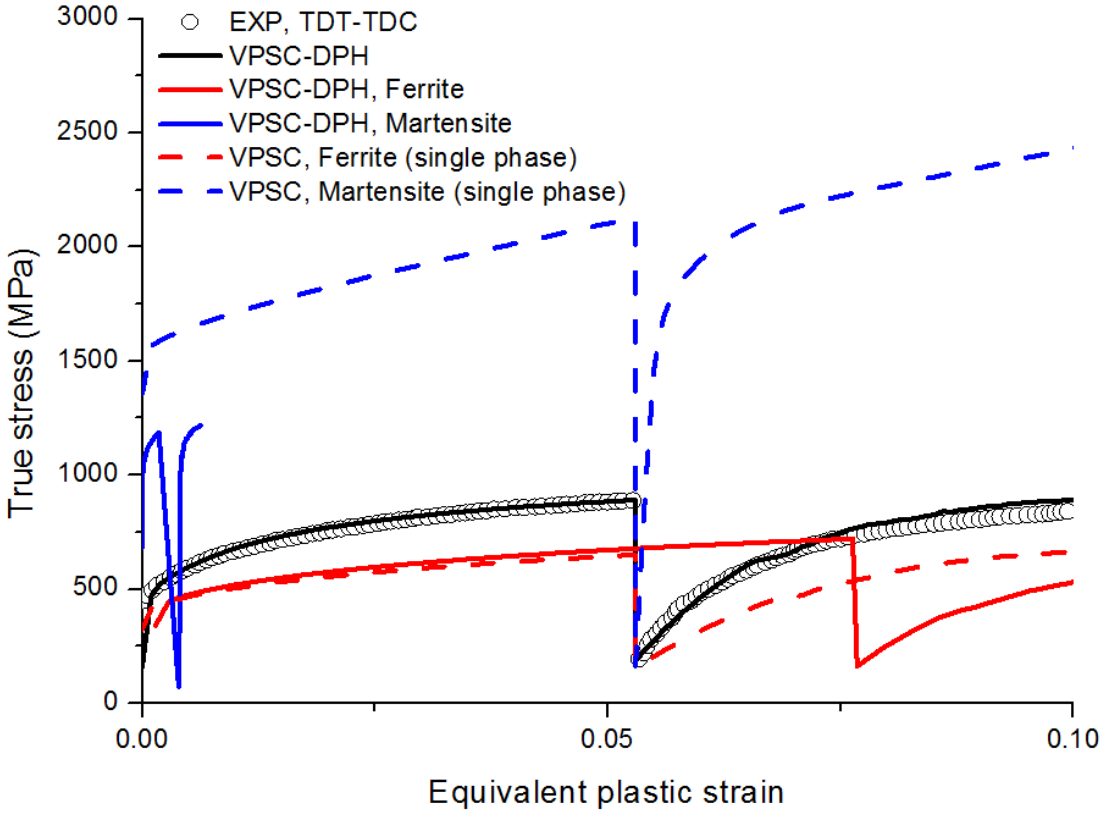

Fig. 17 Stress-strain response of the ferrite and martensite phases. Single phase (dashed line) and dual phase steel (solid line)

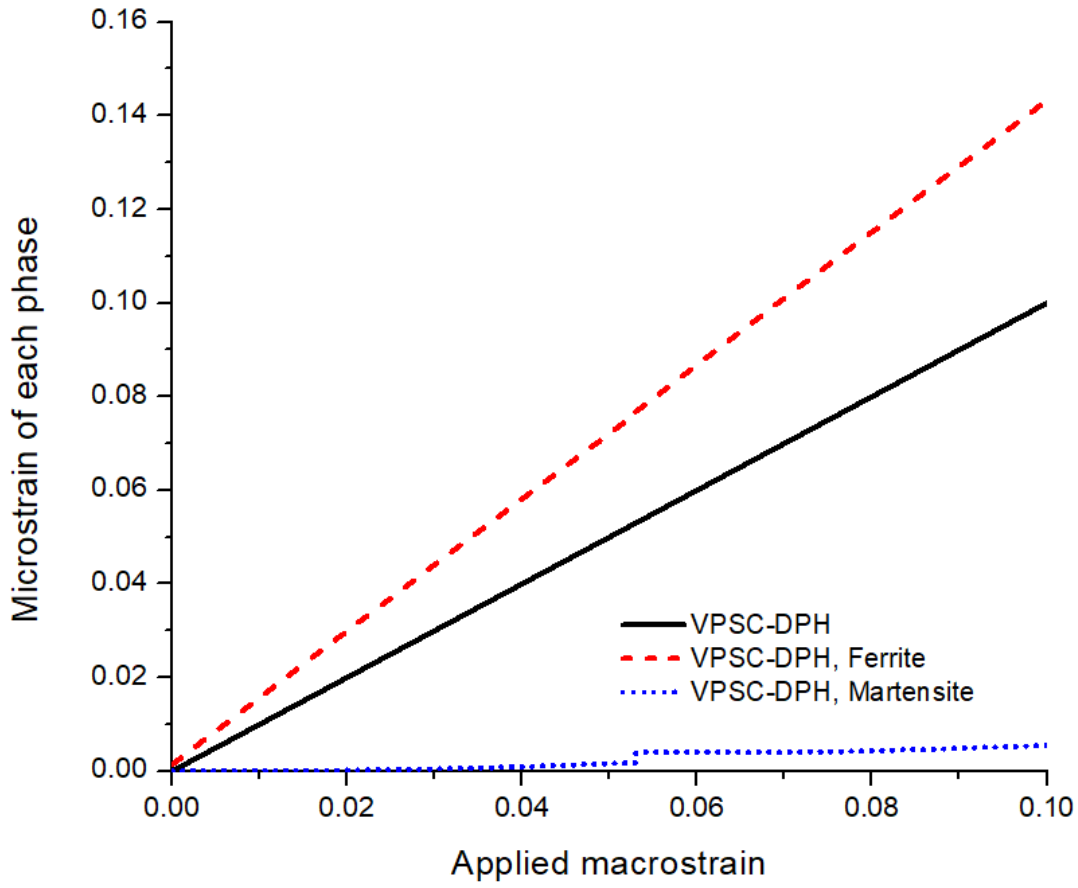

Fig. 18 Strain partitioning of ferrite and martensite as a function of applied strain in dual-phase steel

6.2 Overall predictive accuracy

The predictive accuracy of the VPSC-RGBV model for the flow curve, which can be estimated in Figs. 10 and 11, is somewhat poorer than that of HAH-Yld2000-2d. It should be mentioned, however, that a greater amount of experimental data was used for the characterization of the HAH model. For the VPSC-RGBV model, a single loading path change (i.e., TDT-TDC) was sufficient to provide, at least qualitatively, a reasonable prediction of the stress-strain curves, as shown in Figs. 7, 9, 10, and 11. Furthermore, for certain cases of the r-value evolution, a better accuracy was obtained with VPSC-RGBV than with the HAH model, as illustrated in Fig. 12. It is important to note that experimental r-values were considered for the characterization of the HAH model; however, the VPSC-RGBV model led to better accuracy.

In the metal-forming community, the r-value is used to quantify formability and mechanical anisotropy. Various macroscopic constitutive models suggest the use of the r-value for material identification. Moreover, the yield surface shape is closely related to the r-value according to the associated-flow rule. The r-value evolution shown in Figs. 12 and 13 provides some insights as to how the yield surface shape changes after a change in loading. For instance, the initial fluctuation of the instantaneous r-value, as observed in Figs. 12 and 13, reflects a variation in the yield surface and its normal from the original shape after load change. The initial upsurge in the r-value depends on the magnitude of the strain-path change, as quantified by δ in Eq. (1). In the case of TDT-DDT (δ close to zero), due to the smaller strain-path change, initial fluctuation in the r-value after the strain-path change is less pronounced than in the case of TDT-RDT ($\delta = -0.5$).

In Figs. 14 and 15, the initial yield locus predicted by the VPSC-RGBV model is primarily affected by the crystallographic texture, but not by the RGBV hardening rule. The predictive accuracy of VPSC-SPH on the initial yield surface turned out to be as good as that of VPSC-DPH, as shown in Fig. 15. Therefore, it seems that the *averaged* crystallographic texture can sufficiently represent the initial anisotropy. A possible reason for this observation is that, as indicted in Fig. 6, the initial crystallographic textures of ferrite and martensite are not that different or strong. Although VPSC-

SPH was sufficient for the initial anisotropy, the predictive accuracy of the anisotropic hardening behavior was enhanced by accounting for both the phases. This implies that anisotropic hardening cannot be described well by the initial texture alone. Instead, adequate hardening parameters for separate soft and hard phases are required in the case of multiphase alloys.

After a 6% TDT pre-strain, Fig. 14 shows that the normalized yield surface predicted by the VPSC-RGBV model is in excellent agreement with the experimental data on CHSP45R for all non-proportional strain paths. Although the Bauschinger effect is captured in both VPSC-RGBV and HAH models, the compression yield stress is over-predicted by the HAH model. This is likely because the constitutive parameters of the HAH model were identified with the TDT-RDT and TDT-DDT flow curves. However, it is interesting to note that the VPSC-RGBV model accurately predicts the yield stress in different loading paths with the parameters obtained from the flow curves of TDT-TDC alone.

These results are now discussed in more detail for specific strain-path changes, in particular, for TDT-BT with a stress ratio of 2:1 between the RD and TD axes in Fig. 14. This is a stress state near the cross-loading ($\delta = 0$) and the prediction of the VPSC-RGBV model is in excellent agreement with the experimental yielding point. In the stress-strain curves of CHSP45R (Fig. 10b), the lower reloading yield stress in the case of TDT-DDT, which is also near the cross-loading point, was well predicted, but the subsequent stress overshooting phenomenon was not. The accurate prediction of the yield point in TDT-BT (2:1) is consistent with the accurate prediction of the yield stress after reloading in the TDT-DDT test with a similar strain-path change (similar δ). As the strain increases, due to the very high hardening rate, the yield surface is subjected to latent extension. In other words, it expands rapidly beyond its initial shape in order to produce the stress overshooting that occurs in the experiment (Fig. 10b). This is not possible with the current VPSC-RGBV model. When α^{st} is smaller than α^{ss}, cross-loading contraction occurs and a sudden latent extension phenomenon cannot be achieved. This is because, in the current model, the α^{st} and α^{ss} values are constant and hence these two phenomena cannot be captured at the same time. This seems to indicate that cross-loading

contraction and latent extension are two different phenomena and should be modeled separately. Cross-loading contraction occurs continuously during the pre-straining step while latent extension occurs only after reloading. As a result, the two different mechanisms involve two different models. A latent hardening coefficient α^{st} smaller than the self-hardening coefficient α^{ss} appears to reasonably capture the gradual cross-loading contraction. However, for latent extension, it is more likely that a dislocation treatment is more suitable because the stress-overshooting phenomenon is related to dislocations gliding across a forest. Potentially, the assumption of constant hardening coefficients may not be realistic, since the development of dislocation structure can be affected by a number of microstructural phenomena. Therefore, the hardening matrix based on constant value might need an improvement.

To that end, an extension of the RGBV is required, and may perhaps also be satisfied by an extension of the continuum approach to the level of slip systems, as proposed by Rauch et al. (2011). The use of hardening law featuring two hardening matrices proposed by Luo and Rousselier (2014) can also provide an effective method to capture the evolutionary description on the slip system interactions.

It is worth noting that the current VPSC-RGVB model with the 1-site homogenization may not properly treat multiphase materials with contrasting properties between constituent phases as the dual-phase alloys investigated in the current study. Ideally, either the n-site self-consistent model or the full-field crystal plasticity models might be more suitable for the dual-phase alloy (Canova et al., 1998; Lebensohn, 2001; Sola and Tomé 2001). Therefore, a follow-up study to extend the RGVB model to full-field crystal plasticity model is required to more realistically study the anisotropic hardening behavior of multiphase alloys.

7. Conclusion

In this study, the anisotropic hardening behavior of two different steel sheets subjected to non-

proportional loading was investigated. The materials included a single-phase ferritic steel, CHSP45R, and a dual-phase steel, DP780, consisting of martensite particles embedded in a ferritic matrix. Numerical simulations were performed using a crystal plasticity model, VPSC-RGBV, in which the dynamics of dislocation density evolution are accounted for. In addition, the predictive accuracy of the VPSC-RGBV model was compared against that of the distortional plasticity model HAH.

The mechanical behavior of CHSP45R and DP780 was analyzed using several non-linear strain-path experiments in terms of 1) the stress-strain curves, 2) instantaneous r-value after strain-path change, and 3) yield surface evolution. The main conclusions are summarized below.

1. Although only a single experimental tension-compression (TDT-TDC) test was conducted for the characterization of the VPSC-RGBV model, it shows a predictive capability comparable to that of the HAH model. Considering that more mechanical experiments are required for the identification of the HAH model, the VPSC-RGBV could potentially be employed to provide virtual data as a substitute to costly mechanical parameters.

2. The constitutive parameters of the VPSC-RGBV model were simply identified by numerical optimization using the aforementioned uniaxial tension-compression test data. In spite of using a simple optimization algorithm, the calibrated parameters for each phase of DP780 were physically consistent with literature values calculated by micro-mechanical analyses.

3. The VPSC-RGBV results of DP780 were based on two different sets of discrete orientations: 1) VPSC-SPH by assuming that DP780 is a single-phase BCC structure and 2) VPSC-DPH assuming two separate populations of orientations corresponding to ferrite and martensite. VPSC-DPH showed a better predictive accuracy than VPSC-SPH although VPSC-SPH showed a good predictive accuracy for the initial anisotropy (i.e., initial yield surface) that is governed mainly by the crystallographic texture. The case based on material parameters pertaining to each constituent phase led to improved predictive accuracy. These results suggest that anisotropic hardening cannot be described well by the initial texture alone, but also the phase-specific parameters are required when studying multiphase alloys.

Although the VPSC-RGBV model provides a reasonable accuracy in the prediction of the various mechanical experiments explored in the current study, further research is required to improve the modeling. For instance, the hardening coefficients, which distinguish between cross-loading contraction and latent extension, are fixed as constants, due to which both effects cannot be considered simultaneously (as observed in the case of the CHSP45R steel sheet). As the cross-loading contraction and latent extension are different mechanisms, an extension of RGBV is required by accounting for the evolutionary behavior of the hardening coefficients.

Limitations of the current study is also worth noting. The current VPSC-RGVB model is based on the 1-site homogenization, which might not be suitable for multiphase alloys with contrast properties. To more realistically treat the multiphase alloys, the RGVB approach should be employed to a full field crystal plasticity framework. Also, the current VPSC-RGBV model does not account for elasticity, which is undoubtedly an important factor in multi-phase materials. Thus, an extension of polycrystalline RGBV model to elasto-viscoplastic crystal plasticity framework is required. With this capability, experimental verification using in-situ diffraction becomes feasible, which will provide more direct and precise assessment on the constitutive parameters of multiphase alloys.

Acknowledgments

The authors are grateful to POSCO for generous support. YJ acknowledges the support from National Research Foundation of Korea (NRF-2017R1D1A1B03031052).

References

Al-Abbasi, F.M., Nemes, J.A., 2003. Micromechanical modeling of dual phase steels. Int. J. Mech. Sci. 45, 1449–1465.

Barlat, F., Brem, J.C., Yoon, J.W., Chung, K., Dick, R.E., Lege, D.J., Pourboghrat, F., Choi, S.-H., Chu, E., 2003b. Plane stress yield function for aluminum alloy sheets-part 1: theory. Int. J. Plast. 19, 1297–1319.

Barlat, F., Duarte, J.M.F., Grácio, J.J., Lopes, A.B., Rauch, E.F., 2003a. Plastic flow for non-monotonic loading conditions of an aluminum alloy sheet sample. Int. J. Plast. 19, 1215–1244.

Barlat, F., Grácio, J.J., Lee, M.-G., Rauch, E.F., Vincze, G., 2011. An alternative to kinematic hardening in classical plasticity. Int. J. Plast. 27, 1309–1327.

Barlat, F., Ha, J., Grácio, J.J., Lee, M.-G., Rauch, E.F., Vincze, G., 2013. Extension of homogeneous anisotropic hardening model to crossloading with latent effects. Int. J. Plast. 46, 130–142.

Barlat, F., Vincze, G., Grácio, J.J., Lee, M.G., Rauch, E.F., Tomé, C.N., 2014. Enhancements of homogeneous anisotropic hardening model and application to mild and dual-phase steels. Int. J. Plast. 58, 201–218.

Bergström, Y., Granbom, Y., Sterkenburg, D., 2010. A dislocation-based theory for the deformation hardening behavior of DP Steels: impact of martensite content and ferrite grain size. J. Metall.

Beyerlein, I.J., Tomé, C.N., 2007. Modeling transients in the mechanical response of copper due to strain path changes. Int. J. Plast. 23, 640–664.

Canova, G.R., Wenk, H.-R. and Molinari, A., 1992. Deformation modelling of multi-phase polycrystals: case of a Quartz-Mica aggregate. Acta Metall, Mater., 40, 1519.

Cardoso, R.P.R., Yoon, J.W., 2009. Stress integration method for a nonlinear kinematic/isotropic hardening model and its characterization based on polycrystal plasticity. Int. J. Plast. 25, 1684–1710.

Chaboche, J.L., 2008. A review of some plasticity and viscoplasticity constitutive theories. Int. J. Plast. 24, 1642–1693.

Choi, J., Lee, J., Bae, G., Barlat, F., Lee, M.-G., 2016. Evaluation of springback for DP980 S rail using anisotropic hardening models. JOM 68, 1850–1857.

Chung, K., Lee, M.-G., Kim, D., Kim, C., Wenner, M.L., Barlat, F., 2005. Spring-back evaluation of automotive sheets based on isotropic-kinematic hardening laws and non-quadratic anisotropic yield functions: Part I: theory and formulation. Int. J. Plast. 21, 861–882.

Cong, Z.H., Jia, N., Sun, X., Ren, Y., Almer, J., Wang, Y.D., 2009. Stress and strain partitioning of ferrite and martensite during deformation. Metall. Mater. Trans. A 40, 1383–1387.

Geng, L., Wagoner, R.H., 2002. Role of plastic anisotropy and its evolution on springback. Int. J. Mech. Sci. 44, 123–148.

Ghassemi-Armaki, H., Maaβ, R., Bhat, S.P., Sriram, S., Greer, J.R., Kumar, K.S., 2014. Deformation response of ferrite and martensite in a dual-phase steel. Acta Mater. 62, 197–211.

Ha, J., Lee, J., Kim, J., Lee, M.G., Barlat, F., 2017. Investigation of plastic anisotropy under strain path changes in dual-phase steel using microstructure-based modeling. Int. J. Plast. 93, 89–111.

Ha, J., Lee, M.G., Barlat, F., 2013. Strain hardening response and modeling of EDDQ and DP780 steel sheet under non-linear strain path. Mech. Mater. 64, 11–26.

Hielscher, R., Schaeben, H., 2008. A novel pole figure inversion method: specification of the MTEX algorithm. J. Appl. Cryst. 41, 1024–1037.

Huang, T.T., Gou, R.B., Dan, W.J., Zhang, W.G., 2016. Strain-hardening behaviors of dual phase steels with microstructure features. Mater. Sci. Eng. A 672, 88–97.

Jeong, Y., Barlat, F., Tomé, C.N., Wen, W., 2017. A comparative study between micro- and macro-mechanical constitutive models developed for complex loading scenarios. Int. J. Plast. 93, 212–228.

Khan, A.S., Kazmi, R., Pandey, A., Stoughton, T., 2009. Evolution of subsequent yield surfaces and elastic constants with finite plastic deformation. Part-I: A very low work hardening aluminum alloy (Al6061-T6511). Int. J. Plast. 25, 1611–1625.

Khan, A.S., Pandey, A., Stoughton, T., 2010a. Evolution of subsequent yield surfaces and elastic constants with finite plastic deformation. Part II: A very high work hardening aluminum alloy (annealed 1100 Al). Int. J. Plast. 26, 1421–1431.

Khan, A.S., Pandey, A., Stoughton, T., 2010b. Evolution of subsequent yield surfaces and elastic constants with finite plastic deformation. Part III: yield surface in tension-tension stress space (Al 6061eT 6511 and annealed 1100 Al). Int. J. Plast. 26, 1432–1441.

Kim, H., 2018. A crystal plasticity model for describing the anisotropic hardening behavior of steel sheets during strain-path changes. Doctoral Thesis, POSTECH, Korea.

Kim, J.H., Kim, D., Barlat, F., Lee, M.G., 2012. Crystal plasticity approach for predicting the Bauschinger effect in dual-phase steel. Mater. Sci. Eng. A 539, 259–270.

Kitayama, K., Tomé, C.N., Rauch, E.F., Gracio, J.J., Barlat, F., 2013. A crystallographic dislocation model for describing hardening of polycrystals during strain path changes. Application to low carbon steels. Int. J. Plast. 46, 54–69.

Knezevic, M., Beyerlein, I.J., Brown, D.W., Sisneros, T.A., Tomé, C.N., 2013. A polycrystal plasticity model for predicting mechanical response and texture evolution during strain-path changes: application to beryllium. Int. J. Plast. 49, 185–198.

Kubin, L., Devincre, B., Hoc, T., 2008. Modeling dislocation storage rates and mean free paths in face-centered cubic crystals. Acta Mater. 56, 6040–6049.

Kuwabara, T., Ikeda, S., Kuroda, T., 1998. Measurement and analysis of differential work hardening in cold-rolled steel sheet under biaxial tension. J. Mater. Process. Technol. 80, 517–523.

Lebensohn, R.A., 2001. N-site modeling of a 3D viscoplastic polycrystal using Fast Fourier Transform. Acta Mater. 49 (14), 2723–2737.

Lebensohn, R.A., Tomé, C.N., 1993. A self-consistent anisotropic approach for the simulation of plastic deformation and texture development of polycrystals: application to zirconium alloys. Acta Metall. Mater. 41, 2611–2624.

Lebensohn, R.A., Tomé, C.N., Castañeda, P.P., 2007. Self-consistent modeling of the mechanical behavior of viscoplastic polycrystals incorporating intragranular field fluctuations. Philos. Mag. 87, 4287–4322.

Lee, J.W., Lee, M.G., Barlat, F., 2012a. Finite element modeling using homogeneous anisotropic hardening and application to spring-back prediction. Int. J. Plast. 29, 13–41.

Lee, J.Y., Lee, J.W., Lee, M.G., Barlat, F., 2012b. An application of homogeneous anisotropic hardening to springback prediction in pre-strained U-draw/bending. Int. J. Solids Struct. 49, 3562–3572.

Lee, J.Y., Lee, M.G., Barlat, F., 2011. Evaluation of constitutive models for springback prediction in U-draw/bending of DP and TRIP steel sheets. InAIP Conference Proceedings 2011 Aug 22 (Vol. 1383, No. 1, pp. 571–578). AIP.

Lee, M.-G., Kim, D., Kim, C., Wenner, M.L., Wagoner, R.H., Chung, K., 2005b. Spring-back evaluation of automotive sheets based on isotropic-kinematic hardening laws and non-quadratic anisotropic yield functions: Part II: characterization of material properties. Int. J. Plast. 21, 883–

914.

Lee, M.G., Kim, D., Kim, C., Wenner, M.L., Chung, K., 2005a. Spring-back evaluation of automotive sheets based on isotropic–kinematic hardening laws and non-quadratic anisotropic yield functions, part III: applications. Int. J. Plast. 21, 915–953.

Lee, M.G., Kim, D., Kim, C., Wenner, M.L., Wagoner, R.H., Chung, K., 2007. A practical two-surface plasticity model and its application to springback prediction. Int. J. Plast. 23, 1189–1212.

Luo, M., Rousselier, G., 2014. Modeling of large strain multi-axial deformation of anisotropic metal sheets with strength-differential effect using a Reduced Texture Methodology. Int. J. Plast. 53, 66–89

Mecking, H., Kocks, U.F., 1981. Kinetics of flow and strain-hardening. Acta Metallurgica 29, 1865–1875.

Nelder, J.A., Mead, R., 1965. A simplex method for function minimization. Comput. J. 7, 308–313.

Nesterova, E.V., Bacroix, B., Teodosiu, C., 2001. Experimental observation of microstructure evolution under strain-path changes in low-carbon IF steel. Mater. Sci. Eng. A 309, 495–499.

Ortiz, M., Popov, E.P., 1983. Distortional hardening rules for metal plasticity. J. Eng. Mech. 109, 1042–1057.

Peeters, B., Bacroix, B., Teodosiu, C., Van Houtte, P., Aernoudt, E., 2001a. Work-hardening/softening behaviour of bcc polycrystals during changing strain: Part II. TEM observations of dislocation sheets in an IF steel during two-stage strain paths and their representation in terms of dislocation densities. Acta Mater. 49, 1621–1632.

Peeters, B., Kalidindi, S.R., Teodosiu, C., Van Houtte, P., Aernoudt, E., 2002. A theoretical investigation of the influence of dislocation sheets on evolution of yield surfaces in single-phase BCC polycrystals. J. Mech. Phys. Solids 50, 783–807.

Peeters, B., Kalidindi, S.R., Van Houtte, P., Aernoudt, E., 2000. A crystal plasticity based work-hardening/softening model for bcc metals under changing strain paths. Acta Mater. 48, 2123–2133.

Peeters, B., Seefeldt, M., Teodosiu, C., Kalidindi, S.R., Van Houtte, P., Aernoudt, E., 2001b. Work-hardening/softening behaviour of bcc polycrystals during changing strain paths: I. An integrated model based on substructure and texture evolution, and its prediction of the stress-strain behaviour of an IF steel during two-stage strain paths. Acta Mater. 49, 1607–1619.

Pinard, P.T., Schwedt, A., Ramazani, A., Prahl, U., Richter, S., 2013. Characterization of dual-phase steel microstructure by combined submicrometer EBSD and EPMA carbon measurements. Microsc. Microanal. 19, 996–1006.

Rauch, E.F., Gracio, J.J., Barlat, F., 2007. Work-hardening model for polycrystalline metals under strain reversal at large strains. Acta Mater. 55, 2939–2948.

Rauch, E.F., Gracio, J.J., Barlat, F., Vincze, G., 2011. Modelling the plastic behaviour of metals under complex loading conditions. Model. Simul. Mater. Sci. Eng. 19, 035009.

Schmitt, J.H., Aernoudt, E., Baudelet, B., 1985. Yield loci for polycrystalline metals without texture. Mater. Sci. Eng. 75, 13–20.

Solas, D.E., Tomé, C.N., 2001. Texture and strain localization prediction using a N-site polycrystal model. Int. J. Plast. 17, 737–753.

Stoughton, T.B., 2000. A general forming limit criterion for sheet metal forming. Int. J. Mech. Sci. 42, 1–27.

Vincze, G., Rauch, E.F., Gracio, J.J., Barlat, F., Lopes, A.B., 2005. A comparison of the mechanical behaviour of an AA1050 and a low carbon steel deformed upon strain reversal. Acta Mater. 53, 1005–1013.

Voyiadjis, G.Z., Thiagarajan, G., Petrakis, E., 1995. Constitutive modelling for granular media using an anisotropic distortional yield model. Acta Mech. 110, 151–171.

Weiss, M., Kupke, A., Manach, P.Y., Galdos, L., Hodgson, P.D., 2015. On the Bauschinger effect in dual phase steel at high levels of strain. Mater. Sci. Eng. A 643, 127–136.

Wen, W., Borodachenkova, M., Tomé, C.N., Vincze, G., Rauch, E., Barlat, F., Grácio, J.J., 2015. Mechanical behavior of Mg subjected to strain path changes: experiments and modeling. Int. J. Plast. 73, 171–183.

Wen, W., Borodachenkova, M., Tomé, C.N., Vincze, G., Rauch, E.F., Barlat, F., Grácio, J.J., 2016. Mechanical behavior of low carbon steel subjected to strain path changes: experiments and modeling. Acta Mater. 111, 305–314.

Yoshida, F., Uemori, T., 2003. A model of large-strain cyclic plasticity and its application to springback simulation. Int. J. Mech. Sci. 45, 1687–1702.

Yoshida, F., Uemori, T., Fujiwara, K., 2002. Elastic-plastic behavior of steel sheets under in-plane cyclic tension–compression at large strain. Int. J. Plast. 18, 633–659.

Zaman, S.B., Barlat, F., Kim, J.-H., 2018. Deformation-induced anisotropy of uniaxially prestrained steel sheets. Int. J. Solids Struct. 134, 20–29.